5-2020

Enhancement of Phase Change Material Sorbitol by Nanoparticle Inclusion for Improving Thermal Energy Storage Capabilities

Joshua Kasitz
University of Arkansas, Fayetteville

Enhancement of Phase Change Material Sorbitol by Nanoparticle Inclusion for Improving Thermal Energy Storage Capabilities

Undergraduate Honors Thesis

By

Joshua Kasitz

University of Arkansas

Bachelor of Science in Mechanical Engineering, 2020

Committee Members

Dr. David Huitink, Mechanical Engineering

Dr. Po-Hao Adam Huang, Mechanical Engineering

April 24th, 2020

Abstract

Thermal management of electronic devices has become an increasingly vital field of study with the rapid miniaturization of many key electrical components. With the significant improvement of semiconductor manufacturing and intensified focus on interconnects, electronic devices have decreased in size at an incredible rate. Decreasing spatial requirements is essential to improving device capabilities as the electronic system is able to incorporate more components. Currently, electronic systems are drastically limited by the capabilities of their cooling mechanisms. Smaller devices lead to large increases in the energy density of the system and require more powerful cooling systems to maintain proper component operating temperatures. The cooling systems, heat pipes, fans or vapor/liquid cooling, capable of high performance requirements are often bulky and rely on large energy inputs to remove extra thermal energy, leading to significant reduction in overall system efficiencies. Phase change materials, PCMs, offer an alternative approach to aid in thermal management. PCMs can absorb large amounts of energy, in the form of latent heat, when undergoing a phase transition. This passive cooling mechanism can be combined with conventional cooling systems to protect the system against temperature spikes, allowing the conventional components to be designed for average thermal load rather than peak load.

This study focuses on the enhancement of Sorbitol, a sugar alcohol with a large latent heat (W/g). Many organic PCMs have poor thermal conductivity, an essential component to optimizing a passive cooling system. Previous research shows thermal conductivity and other thermal properties such as melting temperature and latent heat can be changed by altering the materials' crystalline structure through nanoparticle inclusion. Sorbitol naturally has a polycrystalline structure, but it can be shown that dispersed nanoparticles can induce crystalline ordering within the host material's structure. Particle size, type, concentration, and interaction chemistry will be altered in attempt to understand their effect on the thermal properties of Sorbitol. Changes in the composite's structure will be evaluated using a variety of thermal, crystallographic, and mechanical characterization methods. This work covers the trends observed across the thermal and mechanical properties of significance with respect to the alterations in nanoparticle properties. Understanding the effects of nanoparticle inclusion on Sorbitol could lead to the development of property enhancement trends, crucial to optimizing Sorbitol as a PCM for electronic cooling system integration.

Introduction

The focus on phase change materials has increased recently as a potential means to create passive cooling systems. Current passive cooling systems such as heat sinks do not have variable energy removal potential. This means the heat sink must be designed to operate above the highest thermal energy the component will deliver. In many electronic systems temperature spikes, which happen at low frequencies, are the basis for cooling system design. This means the cooling systems are significantly over designed for the average thermal load. PCM offer the potential to reduce the minimum load requirement for the conventional heat removal system by offering temperature spike alleviation. At these high temperatures the PCM will go through phase transition and absorb a large amount of energy. The thermal energy absorbed will slowly dissipate as the PCM cools. In a system combining conventional heat removal with a PCM, the spatial requirements and energy consumption of the heat removal system will significantly decrease. In order to work toward these PCM cooling systems, PCMs themselves must be optimized to achieve the most spatially efficient system. Nanoparticle inclusion in current PCM can lead to thermal enhancements necessary to reduce the size of material needed for these types of

cooling applications. Nanoparticles have been used previously in efforts to improve various thermal properties of PCMs, most commonly in paraffin wax. Introducing nanoparticles causes structural changes to the host material's lattice. This can lead to significant changes in material properties and is the focus of this study. Identifying trends in these changes will lead to a methodology for creating PCM nanocomposites based on electronic component cooling requirements.

Latent heat is a crucial property in energy storage systems. Latent heat is defined as the energy absorbed by a material as it goes through a phase transition. PCM cooling systems rely on the amount of energy they are capable of removing during the phase transition. During this transition, the temperature remains relatively constant. This is crucial to maintaining a low temperature in the electronic component as the PCM is removing energy from the temperature spike. Solid to liquid transitions are the focus of this study and the ideal transition to incorporate into a PCM cooling system. Literature shows nanoparticles can be used to alter this property. It is possible to increase or decrease the latent heat value with respect to the host PCM by using various types and concentrations of nanoparticles. Sorbitol gold nanocomposites were found to increase the latent heat values by upwards of 200% in some cases **Error! Reference source not found.**. The resulting changes in the crystallographic structure resulted in drastic increases of the latent heat values as the nanoparticles forced Sorbitol into a more crystalline form, requiring larger input energy to undergo phase transition. Nanocomposites composed of paraffin wax and iron oxide nanoparticles also showed improvements in latent heat increasing 3.3% and 3.8% with 10% and 20% loading by mass respectively [1]. In another study with various nanoparticle loads of paraffin, Sahan *et al.* found that increasing the concentration of iron oxide nanoparticles corresponds to an increase in the latent heat values [3]. This was attributed to the increase in high surface area to volume ratio of particles dispersed throughout the paraffin structure and the resulting benefits to the strength of the intermolecular interactions [3]. Palmitic acid nanocomposites with titanium oxide nanoparticles show reductions in the latent heat of the sample [4]. Though this is not ideal for creating more efficient PCMs, the introduction of nanoparticles was able to increase the overall stability of the sample. The increase in stability improved the reliability of the sample and improved the amount of melt/freeze cycles it was able to endure without compromising the chemical structure [4]. This work demonstrates the ability to use nanoparticles to alter properties based on application. For the titanium oxide composites, reliability and composite stability needed to improve and an effective PCM was created, even though latent heat decreased by up to 17% [4]. Carbon based nanoparticles have been of high focus recently in PCM nanocomposites in effort to alter the thermal properties. Latent heat generally decreased with the addition of graphene networks, though this was generally expected by the literature. In paraffin wax graphite caused a 12% decrease and multi-walled carbon nanotubes caused a 3.6% decrease in the latent heat value [7]. Carbon-nanotubes also resulted in a latent heat decrease in an expanded pearlite (60 wt%) n-Eicosane (C20) nanocomposite [8]. Graphene oxide led to a 48% decrease in latent heat when combined with paraffin wax [10]. The smallest reduction in latent heat occurred in a paraffin wax and graphene nanoplatelet sample, resulting in 0.7% decrease [12]. Overall, carbon based nanoparticles negatively impacted the latent heat values, but this will be offset by the increase in thermal conductivity. These tradeoffs can be optimized to balance the property augmentations favorably. Iron oxide and gold nanoparticles showed promising increases in latent heat storage capability, though the impact on thermal conductivity was significantly less than that of carbon based materials.

Though PCMs have large latent heats, these organic compounds generally have low thermal conductivities which is a large detriment to a passive cooling system. Thermal conductivity is a metric for characterizing how effectively thermal energy can move through a material. High thermal conductivities result in the best materials for transferring this energy. The PCMs are unable to effectively move thermal energy through their structure and melt over a longer time period as a result [5]. This is not beneficial as it is crucial to swiftly move heat away from the point of generation in electronic components. These components cannot withstand extreme temperature conditions and risk severe damage or risk to life expectancy. Recently, efforts to study nanoparticle effects on sugar alcohols, particularly Sorbitol, have shown the ability to increase the thermal conductivity of the nanocomposites **Error! Reference source not found.**. Sorbitol has a high latent initially, which is vital for effective energy storage, buy lacks the ability to move heat through itself at an efficient enough rate to act as a passive cooling system. Liu *et al.* discovered a 7% increase in the thermal conductivity of Sorbitol with the inclusion of gold nanoparticles **Error! Reference source not found.**. This was achieved with a small loading wt% and is important because it shows the ability to use nanoparticles as a network for transferring thermal energy through a relatively insulating material. Iron oxide nanoparticles have also been used previously to improve the thermal conductivity of paraffin wax [1]. It was demonstrated that iron oxide nanoparticle loading in paraffin wax at 10% and 20% by mass would result in increases of 48% and 60% in thermal conductivity values respectively [1]. In titanium oxide and palmitic acid composite, the nanoparticles led to an increase in thermal conductivity. Palmitic acid does not conduct heat efficiently and the nanoparticles were able to more effectively transfer heat due to their added stability to the sample. This led to improvements in sample reliability. Graphene oxide particles displayed drastic changes in thermal conductivity when incorporated into an organic composite. Carbon nanotubes led to a 113% increase in thermal conductivity for (60 wt%) n-Eicosane (C20) nanocomposite [8]. The type of carbon based nanoparticle was important in the potential for increases in thermal conductivity. In paraffin wax, graphene increased the thermal conductivity 32 fold, while multi-walled carbon nanotubes only increased this value by 11.36 times [9]. Another tested organic compound was docsane, which received a 200% increase of its thermal conductivity with graphene nanoparticles [11]. Graphene oxide resulted in 3.22 times the thermal conductivity when included in paraffin wax [10]. These three particles types all exhibit the ability to improve the thermal conductivity of the sample without inserting significant weight percentages.

Sorbitol was chosen as the PCM for this study because it has thermal properties ideal for use as a phase change material in electronic systems. It has a high latent heat of 250.08 J/g and a melting temperature range of 70 to 80 °C. This melting temperature range fits well within the operating temperatures of electronic systems. Previous demonstrations also showed the thermal properties of Sorbitol can be enhanced with nanoparticle inclusion. Sorbitol is part of a large group of organic polymers called sugar alcohols. This group all exhibit large latent heats but have a variety of melting temperatures ranging from 40 to 250 °C. These alcohols can be homogenously mixed together to form various composites. This significantly alters the thermal properties of the material, specifically the melting temperature. This coupled with nanoparticle inclusion could lead to substantial variability in the electronic systems passive cooling with PCMs could be applied. Future work would focus on the effects of this mixed sugar alcohol composites with nanoparticles, but a strong understanding of the impact nanoparticles have on Sorbitol and why they create these augmentations is needed to move closer toward an effective PCM cooling system. This study focuses on finding present trends in thermal data with respect to nanoparticle properties.

Gold nanoparticles where chosen for multiple benefits they offer. Their success in previous literature is an important indicator of the potential augmentations that can be achieved. Gold nanoparticle inclusion in Sorbitol led to increases in both the latent heat and thermal conductivity, two of the more important thermal characteristics. This previous success signifies opportunities to closely observe these particles to develop trends in the affected properties as a result of the nanoparticles' characteristics. Gold was also chosen because the synthesis method is well proven. This method offers the ability to control the size of the nanoparticle while also introducing a capping agent capable of preventing the nanoparticles from agglomerating. This leads to strong dispersion in the composite. Iron oxide nanoparticles were chosen because previous literature showed they have the potential to create significant increases in thermal conductivity in PCMs. Iron oxide nanoparticles also have convenient synthesis methods that allow another important parameter to be examined. Nanoparticles of the same size can be made through two different co-precipitation methods that result in on set of capped nanoparticles and one set of uncapped nanoparticles. This allows the influence of the capping agent to be observed directly. Graphene oxide nanoparticles were selected because they offer great potential to improve the thermal conductivity by creating a carbon network through the Sorbitol. These nanoparticles are much larger than the previous two and form thin sheet like flakes. It will be important to understand the effect of this shape and particle type on the change in thermal properties.

This study will aim to develop trends in the nanocomposite's thermal properties based on the influence of the nanoparticle's characteristics. These characteristics include nanoparticle size, shape, capping chemistry, particle type, and concentration within the sample. The following lists the goals for this study:

- Find trend in the influence of nanoparticle size and shape on thermal properties (latent heat, melting temperature, and specific heat capacity).
- Determine influence of capping agent on thermal properties (latent heat, melting temperature, and specific heat capacity).
- Develop trend for the impact of nanoparticle type on thermal properties (latent heat, melting temperature, and specific heat capacity).
- Observe the impact of nanoparticle concentration on the thermal properties (latent heat, melting temperature, and specific heat capacity).
- Characterize how the different nanoparticle properties work together to alter the thermal and crystalline properties of the resulting nanocomposite.
- Determine the potential of Sorbitol as a base PCM ideal for cooling applications.

The variability in these parameters should lead to trends that can be used in combination to effectively fine tune the properties of a PCM for implementation into a specific electronic cooling system. This would increase the scope of relevance for PCM passive cooling.

Methods

To achieve effective augmentation of Sorbitol's properties, nanoparticle inclusion must result in a homogenously dispersed nanoparticles. An ideal nanocomposite has evenly spaced nanoparticles so each nanoparticle is affecting a localized region within Sorbitol's structure, while also being isolated from any direct interactions with other nanoparticles. Nanoparticle-nanoparticle interactions cause

significant lapses in sample uniformity where nanoparticle agglomeration drastically reduces dispersion quality, leaving regions of Sorbitol unaffected by nanoparticles. A nanocomposite with these structural inefficiencies will not achieve enhancement of thermal conductivity and will experience reductions in other important thermal characteristics. The nanocomposite will also exhibit gradients in thermal properties across regions that vary from areas of highly concentrated nanoparticles to areas of pure Sorbitol. Creating a homogenous dispersion of nanoparticles can be a difficult task due to the chemical interactions between the nanoparticles and Sorbitol. As a result many options were pursued to optimize the processes by which the final, well dispersed samples were created. The final and successful methods will follow this account and serve as the basis for the samples studied heavily for property alterations.

Nanoparticle fabrication: Gold

Gold nanoparticles were synthesized using the Turkevich method [13]. This method allows for control of the nanoparticle size by altering the trisodium citrate concentrations relative to the gold concentrations in the synthesize process. This process can produce nanoparticles ranging from 9 to 120 nm and can be initiated by increased thermal energy [13]. In this method, reduction of gold chloride (HA_uCl_4) in the presence of trisodium citrate returns well controlled sizing because the citrate caps the gold particles as they precipitate out of the solution and isolates them from forming large clusters or agglomerating into larger particles. Kimling *et al* shows the particle size as a function of concentration ratio of mass between gold and citrate [13]. From this data a curve fit was derived and applied to the fabrication of the nanoparticles used in this experiment. The data supporting this method compares well to other accepted theories describing nanoparticle interactions, such as Mie Theory [13].

The specific steps of the Turkevich method will be outlined with the proper chemical amounts to create 14 nm gold nanoparticles, as used in this study. A curve fit of the data provided by Kimling *et al.* allowed for the concentration ratio to be calculated based off the desired nanoparticle size [13]. The full calculation for this procedure is shown in ***Appendix A***. The concentration ratio needed to achieve 14 nm particles is 0.1978 ($C_{gold}/C_{citrate}$). To start, a 0.01 M solution was created by mixing 197 mg of gold chloride with 50 ml of deionized water. 48.7 ml of deionized water was mixed with 1.3 ml of the gold chloride solution in a 100 ml flask. While stirring with a magnetic stir at 500 rpm, the solution was heated to between 75 and 80 °C using a conventional hotplate monitored with a thermometer suspended in the solution. Separately, the citrate solution was prepared in a second 100 ml flask with 50 ml of deionized water and the 652 mg of trisodium citrate. For other nanoparticle sizes, this citrate mass is altered to obtain the necessary concentration ratio. As the gold chloride solution enters the 75 to 80 °C temperature range, the citrate solution will be added drop by drop until the 10 ml is added. The final solution will continue stirring at this temperature range for 15 minutes, during which the solution should turn a red wine color. The size of the nanoparticles can be confirmed through ultraviolet-visible spectroscopy. The absorption wavelength for 14 nm particles is approximately 522 nm.

Nanoparticle Fabrication: Iron Oxide

Two kinds of iron oxide, commonly referred to as magnetite, particles were used in this study through 2 different co-precipitation techniques. This was done as a means to compare capped and uncapped nanoparticles. The chemistry of the capping agent may be crucial to the changes in Sorbitol's characteristics. These particles were synthesized so the capping agent is the only variance.

The uncapped iron oxide nanoparticles (CIO) were synthesized using a method outlined by Hariani *et al.* This co-precipitation method is regarded as having a 96 to 99% success rate [14]. The co-precipitation requires Ferric chloride ($FeCl_3$), ferrous chloride ($FeCl_2$), and sodium hydroxide (NaOH) [14]. 6.35 g of $FeCl_2$ and 16.25 g of $FeCl_3$ were dissolved in 200 ml of deoxygenated water and stirred for 60 minutes. When 2 M NaOH solution was added in the presence of nitrogen gas at 30 °C and vigorously stirred, iron oxide nanoparticles precipitate out of the solution. The solution was stirred for another 5 hours at 70 °C. To separate the nanoparticles, they were centrifuged, washed with deoxygenated water and stored in solution with deoxygenated water. Figure 1 shows an SEM image of the uncapped iron oxide nanoparticle to show size comparisons. The figure shows the resulting nanoparticles are relatively homogenous in size, approximately 15 nm, with few outliers.

TX-100 capped nanoparticles (SIO) were synthesized using the co-precipitation method outlined by Mandal *et al.* [15]. This method uses ferric ammonium sulfate, ferrous ammonium sulfate and sodium hydroxide to form the magnetite particles in the presence of TX-100. The initial solution was created to contain 0.128 M of Fe (III) and .064 M of Fe (II) ions. This was done by dissolving ferric ammonium sulfate and ammonium sulfate in 100 ml 0.4 sulfuric acid. The second solution was created by adding TX-100 to a 1 M solution of NaOH to achieve a TX-100 concentration of .01 M. This solution was kept between 70 and 80 °C and stirred with a non-magnetic stir. While stirring, 25 ml of the first solution was dropped in. The final solution continued stirring for 30 minutes. Iron oxide nanoparticles settled at the bottom during this time and were rinsed with deionized water before storing as solution in deionized water. The final nanoparticles are shown in Figure 2 through an SEM image.

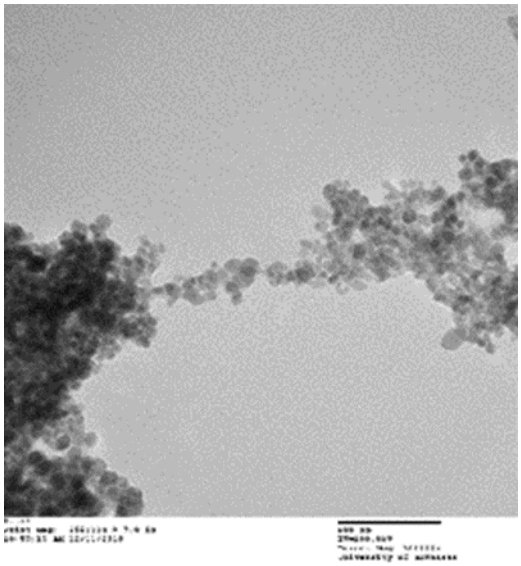

Figure 1. SEM images of uncapped iron oxide nanoparticles with 100 nm scale.

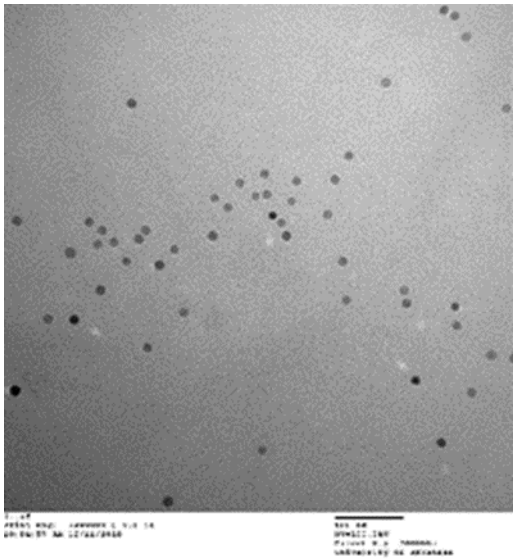

Figure 2. SEM images of TX-100 capped iron oxide nanoparticles with 100 nm scale.

Both types of iron oxide nanoparticles were synthesized to have the same size of 15 nm. The SEM images in Figure 1 and Figure 2 support successful co-precipitations as most particles are approximately 15 nm and all are close to this size, given error considerations of fabricating significant quantity of nanoparticles. Through the images the impact of the TX-100 as a capping agent can be visibly seen. The uncapped particles in Figure 1 have collected together due to the interactions between particles. This differs significantly from the TX-100 capped particles in Figure 2 which do not display signs of

agglomeration. This phenomena should lead to nanocomposites with capped particles resulting in higher dispersion qualities.

Nanoparticle Fabrication: Graphene Oxide

Graphene oxide has a significantly different structure than gold or iron oxide nanoparticles. Rather than forming in a spherical shape, graphene oxide forms in thin sheets that agglomerate by stacking on top of each other. Graphene oxide was chosen because literature has shown the ability of graphene oxide nanoparticles to increase the thermal conductivity of a system successfully.

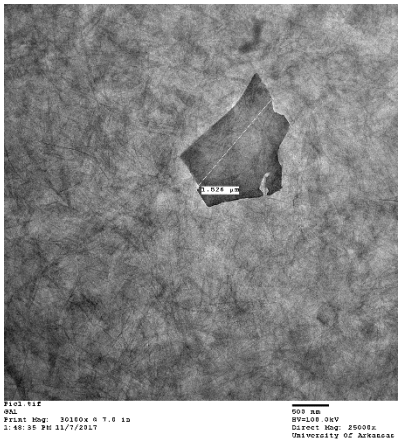

Figure 3. TEM image of Graphene Supermarket GO NP with 500 nm scale.

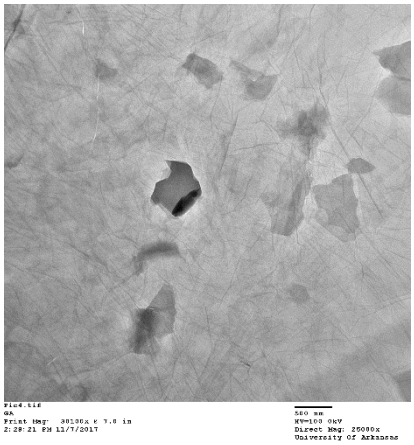

Figure 4. TEM image of Graphenea GO NP with 500 nm scale.

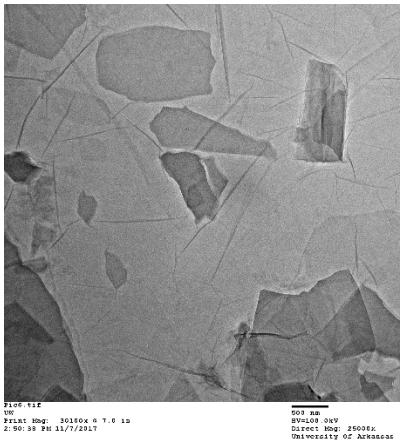

Figure 5. TEM image of University Wafer GO NP with 500 nm scale.

Three different graphene oxide nanoparticles were purchased with the intent of varying the size and concentration in the nanocomposites. All three samples are initially in solution with deionized water. Graphene Supermarket (GS) was the provider for the smallest nanoparticle size. These particles have sizes ranging from 0.5 – 5 μm. TEM images shown in Figure 3 support the size range for these nanoparticles. Nanoparticles from supplier Graphenea (GA) have sizes less than 10 μm. Figure 4 shows one of the TEM images supporting the size range for the Graphenea particles. The largest particles were obtained from University Wafer (UW) and have particle sizes less than 15 μm. The size range of these particles is supported by the TEM image in Figure 5. The details of the graphene oxide nanoparticles are given in Table 1 along with the sample abbreviation that will be used to identify nanocomposite types and the carbon approximate carbon content percentage of the nanoparticles.

Table 1. Graphene Oxide nanoparticle summary.

Particle Abbreviation	Supplier	Carbon Content %	Size
GS	Graphene Supermarket	79%	.5-5um
GA	Graphenea	49-56%	<10um
UW	University Wafer	49-56%	<15um

As previously mentioned the graphene oxide nanoparticles were unsuccessful in homogenously dispersing in Sorbitol. The strong polar nature of the nanoparticles caused them to attract more effectively to each other than the sorbitol molecules, even though the Sorbitol molecule is also polar. As

a result, the nanoparticles needed a capping agent to surround the nanoparticle and protect it from agglomeration. Trisodium citrate ($Na_3C_6H_5O_7$) is the capping agent that leads to a strong dispersion quality in the nanocomposites. This capping agent has a high molecular weight of 258.06 g/mol and a high melting temperature of over 300 °C, which is substantially over the melting range of the Sorbitol nanocomposites. The high melting temperature is important so the capping agent does not melt before the host matrix does, preventing the capping agent from changing shape around the nanoparticles. The graphene nanoparticles are capped using the following process. First, 5 ml of deionized water is added to a skinny beaker. Trisodium citrate, in powder form, is added to the DI water based on the mass of nanoparticles being add to the final solution. For every 1 gram of nanoparticles, 1167.17 g of trisodium citrate is needed. The powder and water mixture is sonicated for 15 minutes, or until completely dissolved. The desired amount of the nanoparticle solution is added and the final solution is sonicated for 15 minutes, or until completely dissolved. The final solution should be homogenous and have a brown-purple translucent color. At this point the nanoparticles have been capped and are ready to be added to Sorbitol.

Sorbitol Solution Setup

D-Sorbitol was purchased from Sigma-Aldrich in powder form, rated at greater than 98% purity. To effectively mix the nanoparticles with Sorbitol, it must be in solution state. To achieve this, Sorbitol is sonicated with deionized water at the solubility limit of Sorbitol in water, 2.35 g/ml. The sonication period is 60 minutes, or until the Sorbitol is completely dissolved. Figure 6 shows the sonication process of the deionized water and white Sorbitol powder mixture prior to completion. The resulting solution will be translucent and have a noticeably higher viscosity. The dissolved solution is stable and has a shelf life exceeding 6 months, assuming the solution's integrity is not compromised.

Figure 6. Sonication of Sorbitol solution.

Nanocomposite Fabrication

The nanocomposite is created by combining 10 ml of the Sorbitol solution with the particular nanoparticle solution for each different nanocomposite. This quantity will produce a cylindrical sample with a height of 0.5" and diameter of 0.75". The mixture is sonicated for 15 minutes, or until the solution is a homogenous translucent color. This color will depend on the nanoparticles and the fullness will

correlate to the particle concentration. Gold nanoparticles will create a red wine hue, graphene oxide will create a brown hue, and iron oxide will create a burnt orange or rust shade. The samples will remain these colors even after the curing process.

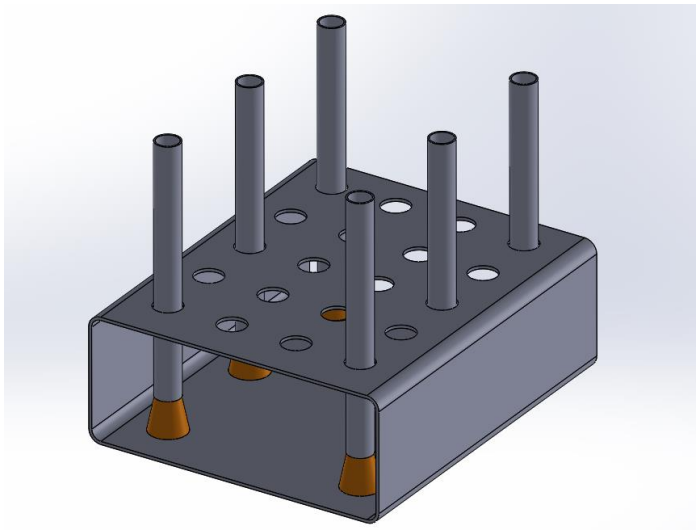

Figure 7. Sample Curing stand and curing tubes.

The final solution must undergo a curing phase to remove all the water from the solution. Water negatively impacts the crystalline structure of the material as it forms hydrate phase when in contact with the nanocomposite. The hydrate form does not exhibit the impressive thermal properties of Sorbitol and is therefore undesirable in the composite. Each sample is cured for 96 hours to confirm all water has been baked out of the solution. Figure 7 shows a model of the curing apparatus constructed to hold the solution. The stand and tubes are aluminum. The orange stoppers are high temperature silicon rubber. The stopper forms a seal at the base to prevent sample leakage, but also allows easy removal of the sample. The curing process occurs at 140 °C, which is well above the melting temperature of any Sorbitol crystalline phase. This ensures the solution will not trap any water by prematurely solidifying during curing.

After cooling, the sample is allowed to cool for 24 hours to ensure complete crystallization within the sample curing tubes. When cooled the rubber stopper is removed from the curing tube. The nanocomposites resist adhering strongly to the stopper so it can be pulled out with little resistance. To remove the sample from the tube the, a rod is used to push the sample out under the presence of heat. The sample adheres strongly to the aluminum tube. Using a heat gun, the tube surrounding the sample is heated to soften the sample-tube interface before the sample is able to be pushed out. The cylindrical sample will be stored in a dry box to minimize contact with water vapor, thus limiting hydrate formation.

Sample	Conc. NP g/ Sorbitol g	Nanoparticle Size	Capping Agent
S1	0	NA	NA
CIO-H	6.01E-06	~15 nm	Uncapped
CIO-M	2.55E-06	~15 nm	Uncapped
CIO-L	3.40E-07	~15 nm	Uncapped
SIO-H	6.01E-06	~15 nm	TX-100
SIO-M	2.55E-06	~15 nm	TX-100
SIO-L	3.40E-07	~15 nm	TX-100
Au-H	6.01E-06	14 nm	Trisodium Citrate
Au-M	2.55E-06	14 nm	Trisodium Citrate
Au-L	3.40E-07	14 nm	Trisodium Citrate
GS-H	2.91E-05	.5 - 5 µm	Trisodium Citrate
GS-M	1.50E-05	.5 - 5 µm	Trisodium Citrate
GS-L	8.26E-06	.5 - 5 µm	Trisodium Citrate
GA-H	2.91E-05	< 10 µm	Trisodium Citrate
GA-M	1.50E-05	< 10 µm	Trisodium Citrate
GA-L	8.26E-06	< 10 µm	Trisodium Citrate
UW-H	2.91E-05	< 15 µm	Trisodium Citrate
UW-M	1.50E-05	< 15 µm	Trisodium Citrate
UW-L	8.26E-06	< 15 µm	Trisodium Citrate

Figure 8. Final sample list.

The final samples of interest are shown in Figure 8. These samples have well dispersed nanoparticles and will be studied for their thermal and crystallographic properties. CIO and SIO denote the uncapped and TX-100 capped nanoparticles respectively. The gold samples are Au. GS, GA, and UW represent the 3 different particle sizes for the graphene oxide nanoparticles.

X-Ray Diffraction

Crystallographic data was collected using the Rigaku MiniFlex X-Ray Diffractometer. This machine had a 30 kV – 15 mA x-ray and utilized a Kb filter. The machine has a scattering of 4.2 degrees and a receiving slit of 0.3 mm. The continuous scanning tests were run from 5 to 45 degrees with a step interval .02 degrees to fully cover the main crystalline peaks in Sorbitol. For the sample preparation, metal coupons with square holes cut through the center were taped to a glass slide and placed on a hot plate. The sample was fully melted on the glass slide and allowed to cool for 24 hours. The glass slide was then removed, leaving a thin composite sheet that could be tested.

Ultraviolet-Visible Spectroscopy

The UV-vis measurements were obtained using a DU 730 UV/Vis Spectrophotometer from Beckman Coulter. The machine was calibrated using deionized water as the reference sample before each test. Due to the translucent nature of these nanocomposites, thin samples can be measured using this technique successfully. These samples were prepared in the same fashion as done for XRD. This technique was primarily used to confirm the nanoparticle size of gold synthesis, but was also used to compare the changes in peak absorption between similar particle samples. The results are not directly displayed in this paper, but they were impactful in early efforts to effectively disperse iron oxide and graphene oxide nanoparticles homogenously in Sorbitol.

Differential Scanning Calorimetry

Most of the thermal experiments conducted in this study were done using a DSC 25 by TA Instruments. Differential scanning calorimetry is a technique which measures the heat input required to increase the temperature of a sample. In these experiments the reference with which this is measured against is air sealed in the sample holder. The tested samples were created by crushing the sample into powder and adding between 8 and 9 mg into the test pan. The test pans were all hermitically sealed. Figure 9 shows the DSC 25 and Figure 10 shows a test pan setup to run a thermal test with the top pan as the reference sample and the bottom pan as the hermetically sealed test sample.

Figure 9. DSC 25.

Figure 10. Sample setup for DSC.

Latent heat, melting temperature, and specific heat were collected using the DSC. The test to find the latent heat was setup as follows. The sample was equilibrated at 10 °C before undergoing a temperature ramp of 3 °C per minute until the sample reaches 130 °C. The sample's temperature is then ramped back to 10 °C at the same ramp rate. This test plots the heat flow into the sample as a function of temperature. The melting temperature for this study is defined as the temperature at the peak heat flow and is accompanied by melting ranges to signify the start and end of the melt. Latent heat can be extracted from this graph as the area under the curve.

The second test provides the data to obtain the specific heat of the sample with respect to its temperature. The sample equilibrates at 10 °C and ramps to 130 °C at a ramp rate of 2 °C per minute with a reversing heat flux. The specific heat capacity is plotted as a function of temperature, where points of emphasis are before the melt, solid state, at 35 °C and after the melt, liquid state, at 100°C.

Visible Characterization Techniques

The techniques outlined in this section were used for as qualitative sample preparation methods. They helped distinguish the quality of the sample preparation, with results not directly reported here. Qualitatively it could be determined whether the sample achieved a strong dispersion. Visually the samples were inspected to identify regions of particle agglomeration, if any.

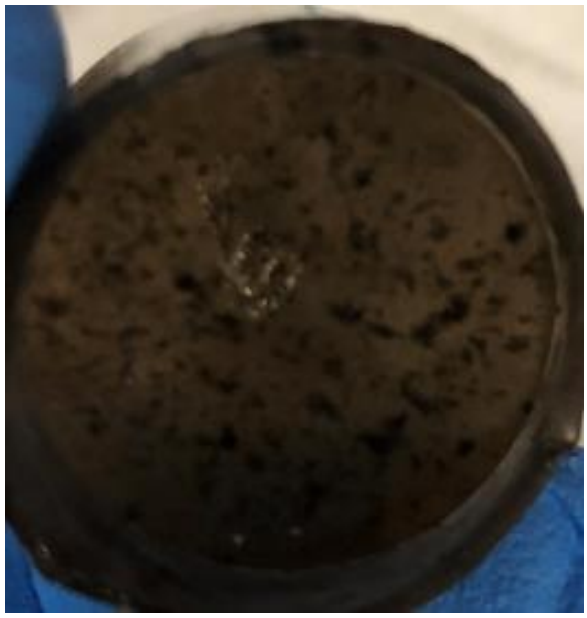

Figure 11. Graphene oxide nanocomposite with poor dispersion.

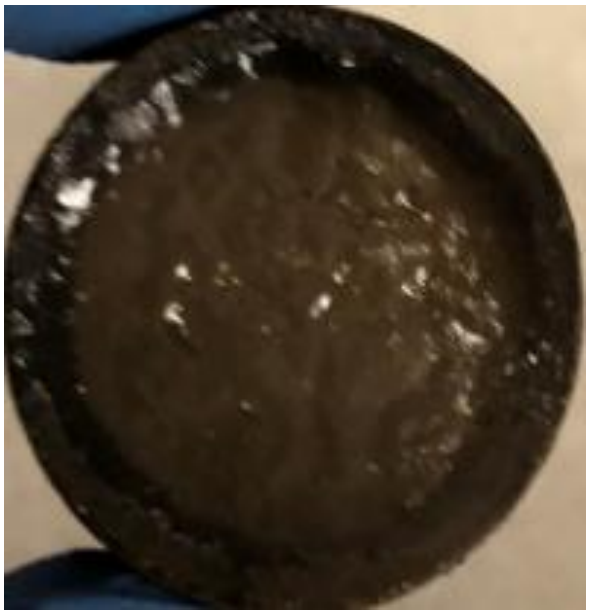

Figure 12. Graphene oxide sample with strong dispersion (GA-L).

The samples shown in Figure 11 and Figure 12 represent the visual differences that can be seen in samples with poor and strong dispersion of nanoparticles for graphene oxide samples. Figure 11 shows a sample that lacked enough trisodium citrate to effectively cap the nanoparticles and prevent them from agglomerating. Figure 12 shows the impact of the correct capping agent concentration for graphene oxide and is the GA-L sample used in the final testing. Samples were also observed for mechanical characteristics such as their hard and brittle nature. Successful samples were brittle in nature, while many samples with too much trisodium citrate resulted in pliable samples resembling putty.

Samples were also observed with the light microscope on a XE7 AFM from Park Systems. The microscope has a magnification of 10x. Samples were observed using this microscope to visualize the structural differences between various composites. Samples for this observation were prepared using the same methods as described for XRD to obtain thin and flat samples. These images were used to support other visual characterization techniques used.

The aforementioned techniques were used to determine the success of the sample preparation process and were used in the initial sample design phase. Graphene oxide was particularly difficult to disperse in Sorbitol. These techniques were used to identify the effect of various capping agent types and concentrations until a proper sample formula was developed, with which the final samples were created. The final sample set qualitatively reflects strong dispersion so the influence of the nanoparticles can be directly observed without obstruction of sample impurities such as particle collection.

Results

X-Ray Diffraction

The influence of the nanoparticles can be seen by observing the crystalline change in the new nanocomposite. This is represented using x-ray diffraction to determine the magnitude of the effect created by the nanoparticles. Using Bragg's Law, $n\lambda = 2dsin\Theta$, the change in lattice spacing can be determined from the change in peak location along the scan in degrees. The shift in peaks relative to the control sample is used to determine the lattice shift. Table 2 shows the samples that will be examined for crystalline changes.

Table 2. XRD sample list.

Sample	Nanoparticle Size	Capping Agent	Conc. NP g/ Sorbitol g
S1	NA	NA	0
GA-L	< 10 µm	Trisodium Citrate	8.26E-06
Au-7	30 nm	Trisodium Citrate	9.77E-06
CIO	15 nm	Uncapped	2.42E-05
SIO	15 nm	TX-100	2.42E-05

The changes are based off the results from the original sample structure. Figure 13 shows the plot for the control sample, Sorbitol. The peaks in this figure are numbered to show how they correspond with phase preference order. Higher peaks denote a more significant phase, meaning a higher order of crystallinity is present for that particular phase relative to others. ***Appendix B*** shows the raw data for determining the impact of nanoparticles on the lattice spacing using Bragg's Law. The phase number is listed in these charts to help show the where the changes are committed between samples. This is done for each particle type with respect to the control sample.

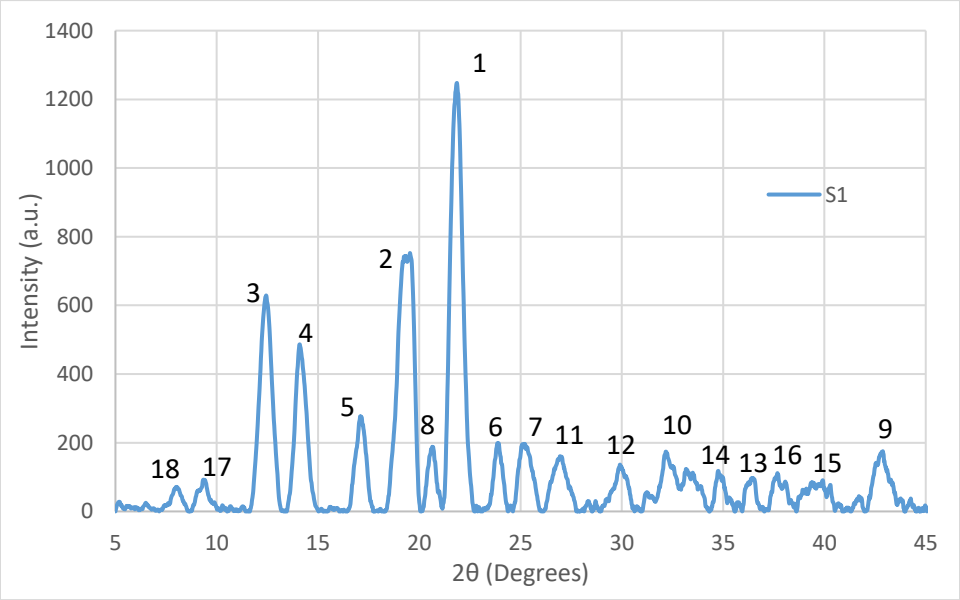

Figure 13. XRD plot for plain Sorbitol showing peak numbers.

The following will demonstrate the changes in the lattice spacing with respect to the control sample and detail significant changes and newly introduced phases derived from nanoparticle inclusion. Figure 14 will show a visual representation of the shift in peaks for all samples. Individual comparisons between control and each different nanoparticle sample are shown in ***Appendix C***. It is important to note, the intensity of the peak is an arbitrary unit and is not used to compare intensity between different samples.

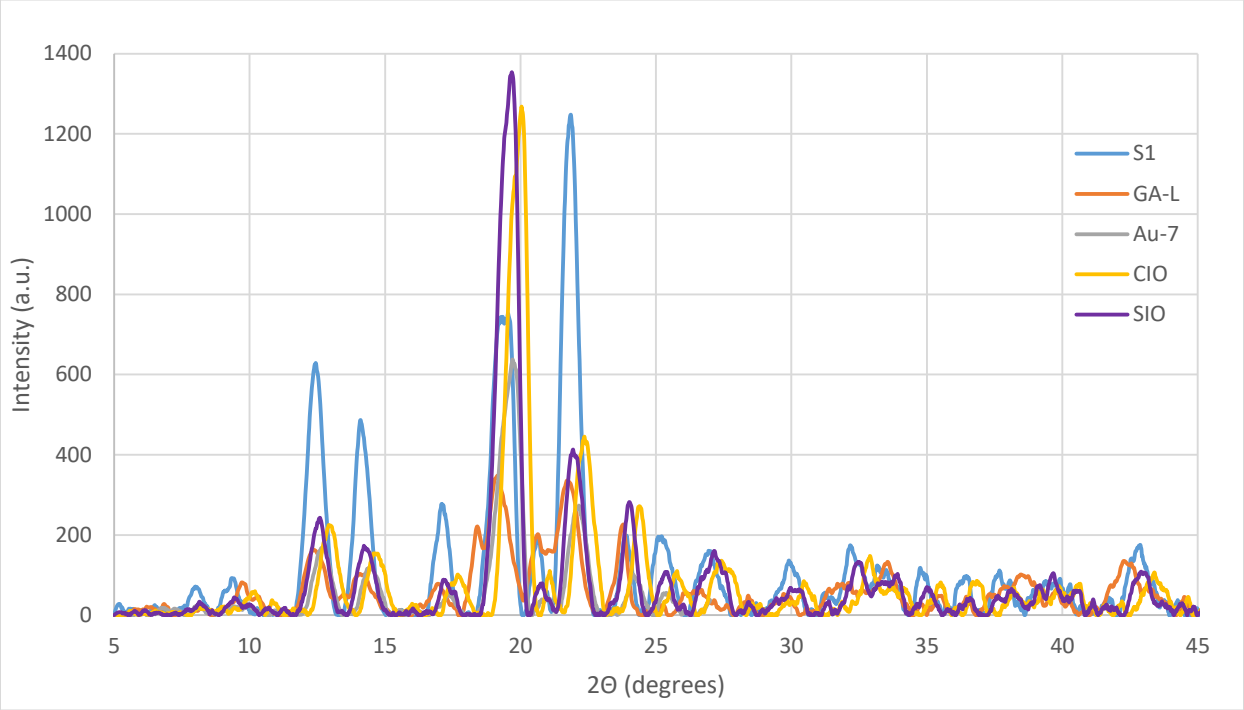

Figure 14. XRD Plot for nanocomposite comparison.

As seen in Figure 14, most of the phases in the nanocomposites resemble those seen in the control sample. These peaks have shifted due to the stretching of the lattice caused by the nanoparticles. There are a few cases where a control peak does not occur in the nanocomposite. This is seen in the lower preference, weaker peaks. The more prominent peaks are present in the nanocomposites.

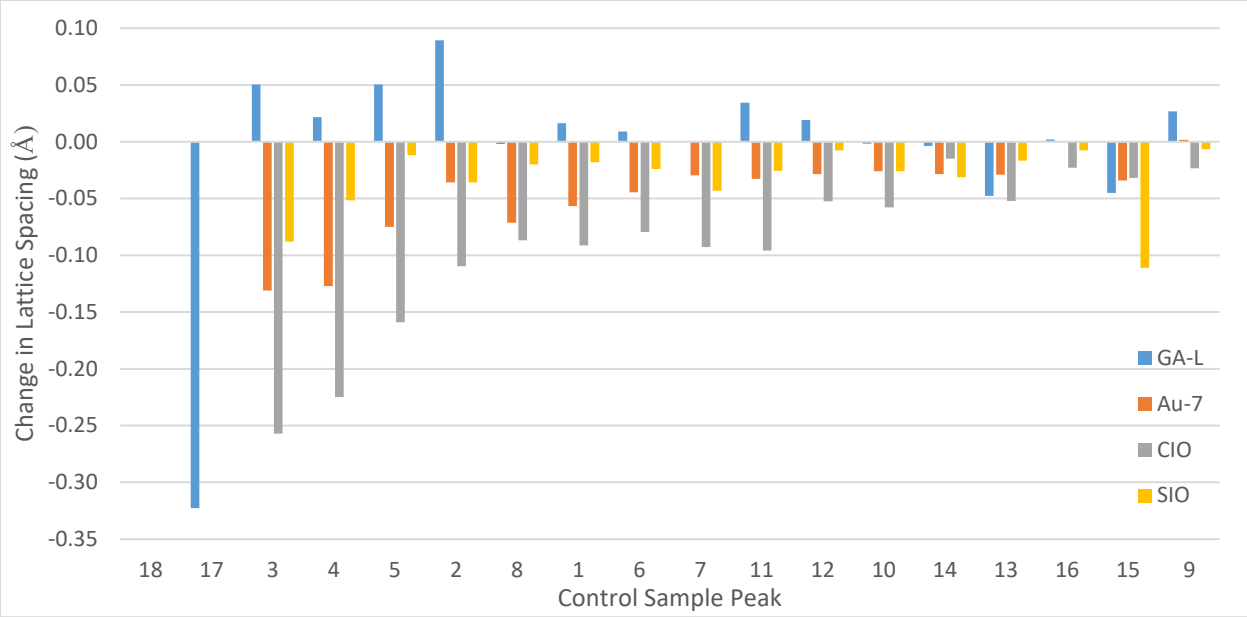

Figure 15. Change in lattice spacing with respect to control Sorbitol for distinguishable peaks.

Influences of nanoparticle inclusion can be directly related to the change in the lattice spacing. As the nanoparticles are inserted into the host matrix, localized regions will stretch or shrink depending on their proximity to the nanoparticle. This will lead to an overall change in the lattice spacing of major phases, indicated by peaks on XRD plots. From Figure 13, 18 Sorbitol peaks were identified and will observed in the nanocomposite samples. Figure 15 shows the change in lattice spacing. This value is the nanocomposite spacing minus the control spacing. A few sorbitol peaks did not have defined peaks present in the nanocomposite samples. Peak 18 was only present in control Sorbitol. Peak 17 was seen in the graphene oxide sample, but was not present in the iron oxide and gold samples. Peaks 16 and 9 had the uncapped and TX-100 iron oxide samples, but not the gold and graphene oxide samples.

Gold nanoparticles caused a shift to the right in the XRD plot, higher angle location of the phase. This lead to a reduction of the lattice spacing in the overall composite at each peak. The average decrease in the lattice spacing was 0.0499 Å and the maximum change was 0.1310 Å. The gold nanoparticles are small and spherical. As a result, each particle affects a small localized region within the composite and is not too far from its neighboring nanoparticles. The uniformity of this nanoparticle dispersion, leads to compression of the lattice spacing with respect to control Sorbitol. The host matrix must shrink in localized regions to accommodate the nanoparticles. It appears there is a weak relationship between the prominences of the phase and the, magnitude with which the lattice spacing is affected. This makes sense because of the polycrystalline nature of sorbitol. Larger phase presence leads to the ability for the nanoparticles to make a greater impact on the spacing of that particular phase. The larger phases are consistent in structure over much greater areas. Less prominent phases occupy less of the total composite and will not see as the same level of influence. The smaller phases have less uniformity through the middle of their grain and are affected more significantly by the boundaries of their region. Large grains do not receive the same percentage of influence from boundaries. Interestingly, some of the weaker phases were not present in the gold nanocomposite. It is possible the gold nanoparticles forced Sorbitol to not form some of these peaks as the composite forms more of the crystalline phases.

Both of the iron oxide nanoparticles also decreased the lattice spacing. The TX-100 nanoparticles did not have the same impact as the uncapped nanoparticles. The uncapped nanoparticles created an average decrease of 0.0908 Å with a maximum of 0.2571 Å. This was 3 times as large as the TX-100 capped nanoparticles affect which led to an average decrease of 0.0328 Å, with a maximum of 0.0879 Å. Since the nanoparticles are the same size, this difference must result from the different capping agents. The uncapped particles agglomerated at a higher rate than the TX-100 capped as seen in Figure 1 and Figure 2. A few particles attracted to each other would create a greater disturbance in the lattice than a single particle. The uncapped nanoparticles may have created small collections, possibly just a few particles that extended a greater compressing effect on the surrounding lattice than the singular caped particles. This is one option for why this phenomena occurs, but the effect of the capping chemistry interacting with Sorbitol could also play a significant role. The TX-100 capped may interact with the Sorbitol in such a way to reduce the change in spacing. Though the exact interactions leading to the difference in lattice spacing is not clear, it can be determined that the capping chemistry plays a crucial role in altering the lattice structure. Two identical particle types and sizes created responses with very different magnitudes as a result of different capping interactions.

The graphene oxide nanoparticles resulted in trends completely different than the other samples. This was the only sample where the lattice spacing increased. Approximately half of the samples saw increases in the lattice spacing as a result of the graphene oxide nanoparticles. This is not what is expected. The average change in lattice spacing was a decrease of 0.0069 Å, which is an order of magnitude smaller than the other particles. The maximum increase in lattice spacing was .0504 Å and the maximum decrease was 0.0450 Å. Typically the nanoparticles would cause the localized regions around them to be compressed, leading to a decrease in the lattice spacing. This shows the graphene oxide flakes do not interact with the sorbitol matrix in the same way as either gold or iron oxide does. The drastic difference in size may be the cause of this interaction. The large graphene oxide flakes are on the order of microns and are affecting a larger area per particle. There are also significantly less graphene oxide particles, compared to gold or iron oxide. This means there are larger distances in the composite between each nanoparticle. In this larger distances, the lattice spacing is not impacted. Shape could play an important role in this phenomena as the graphene oxide nanoparticles are sheet like flakes. These will interact in very different ways compared to a conventional spherical shape. Though it can be inferred the shape and size of the nanoparticle has great impact on the influence of the nanoparticle on the lattice structure, the exact interaction between Sorbitol and nanoparticle are not completely understood. There is still significant data collection needed to understand the scope of these interaction in effort to interpret a clear trend.

Peak Heat Flow & Melting Temperature

Often, polycrystalline materials do not have an exact melting temperature, but instead melt over a temperature range. This occurs because the polycrystalline material has multiple phases, each with their own respective melting temperature. This leads multiple peak heat flows, each defining the melting temperature of a specific phase. Heat flow peaks shown on these thermal plots will correspond to prominent phases in the composite. Phases with weak presences will not record discernable peaks, but may affect the width and depth of the peaks. The resulting effect can be observed in the gold heat flow data shown in Figure 16.

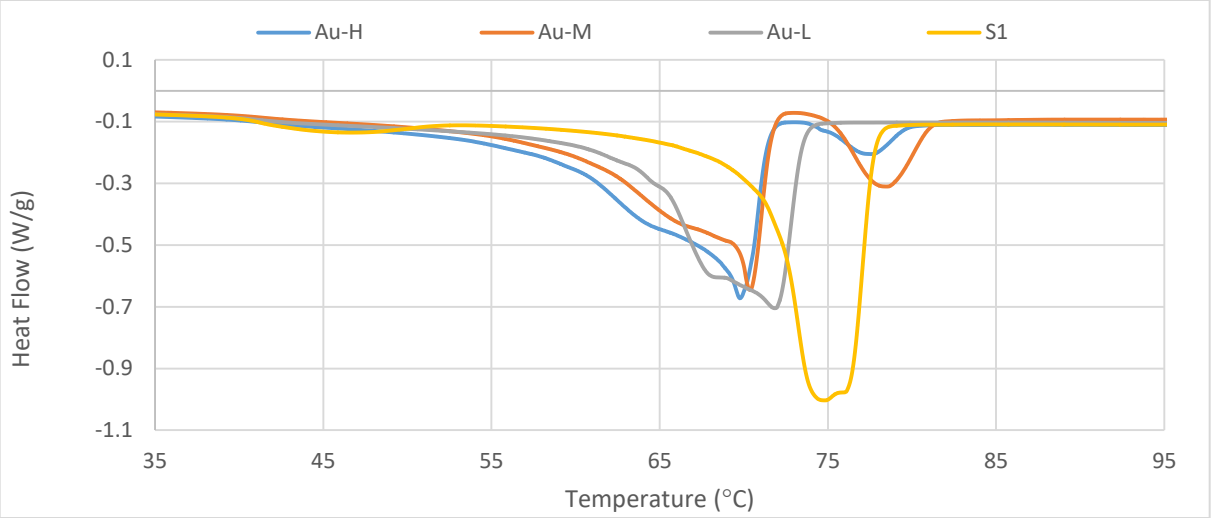

Figure 16. Au nanocomposite heat flow vs temperature.

The strength and temperature of the peak heat flow can be related to the crystallographic structure. Control Sorbitol has two more prominent phases as demonstrated earlier in Figure 13. These phases have similar lattice spacing as shown by Bragg's Law. This corresponds to the two peak heat flows seen in the Sorbitol sample as both phases exhibit approximately the same heat flow and melting temperatures that only differ by a few degrees. Gold nanoparticles alter the phases naturally formed by Sorbitol, changing the lattice spacing and prominence of each phase. This is evident in the gold samples as even the lowest concentration of gold significantly changed the melting temperatures of the prominent phases. Higher concentrations of gold nanoparticles induced another prominent melt in the composite at approximately 78 °C. This indicates the presence of a new phase that is not prominent in the control sample and indicates the importance of concentration on controlling the crystallographic structure.

Table 3. Peak Heat Flow and Melting Temperature values for gold nanocomposites.

Melting Temperatures (°C)

Sample	Peak Melt	Secondary Melt	Tertiary Melt	Total Melt Range
S1	74.77	76.06	NA	19.83
Au-H	69.78	64.56	77.42	32.77
Au-M	70.38	66.50	78.33	33.68
Au-L	71.84	68.12	NA	22.94

Peak Heat Flows (w/g)

Sample	Peak	Secondary	Tertiary
S1	0.959	0.975	NA
Au-H	0.647	0.438	0.205
Au-M	0.639	0.433	0.310
Au-L	0.672	0.602	NA

Table 3 presents the values for each of the 3 different melts in the gold nanocomposites. From this table it can be seen that increasing the concentration of gold nanoparticles will lead to a decreasing melting temperature for each respective phase. The total melt range is significantly larger in samples with high

gold nanoparticle concentration because these samples introduced a third melt at higher temperature than the peak melt.

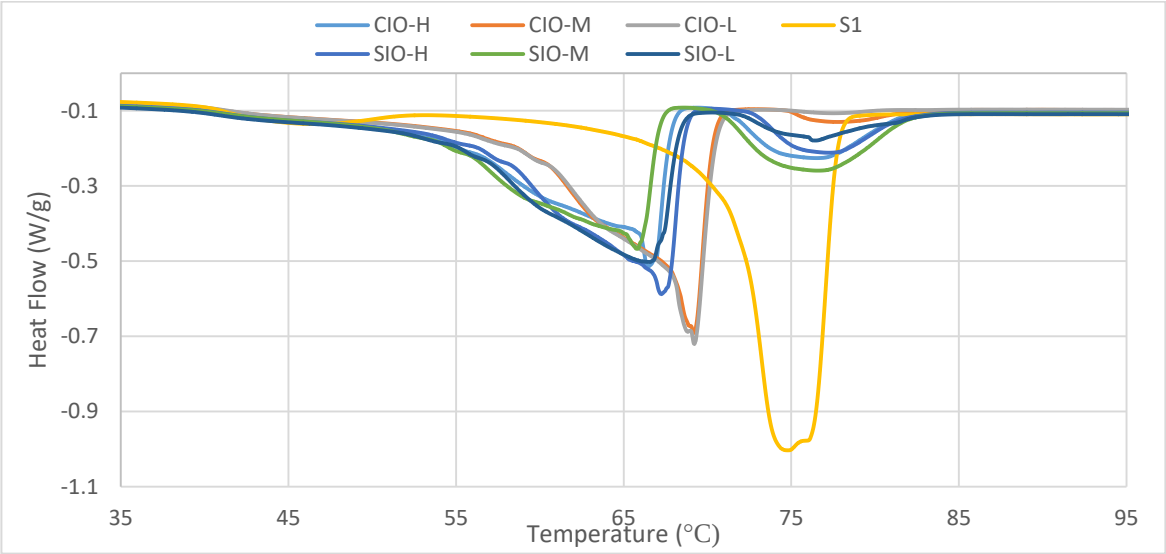

Figure 17. Heat flow vs temperature for iron oxide nanocomposites.

As shown in Figure 17, both uncapped and TX-100 capped iron oxide nanocomposites demonstrate significant changes in the melting temperatures and peal heat flows of the composite, signaling a change in the preference and characteristics of the crystalline phases. Like gold, the iron oxide induces a prominent phase with a melting temperature around 77 °C, depending on concentration. The significant changes in the original two peak heat flows represent changes to the lattice spacing of the composite created by the nanoparticles.

Table 4. Peak heat flow and melting temperature values for iron oxide nanocomposites.

Melting Temperatures (°C)

Sample	Peak Melt	Secondary Melt	Tertiary Melt	Total Melt Range
S1	74.77	76.06	NA	19.83
CIO-H	66.44	64.40	76.42	40.14
CIO-M	69.18	68.86	77.97	40.69
CIO-L	69.21	68.76	77.60	36.60
SIO-H	67.27	65.35	77.33	37.88
SIO-M	65.79	64.77	76.69	40.18
SIO-L	66.54	60.34	76.33	40.60

Peak Heat Flows (W/g)

Sample	Peak	Secondary	Tertiary
S1	0.959	0.975	NA
CIO-H	0.511	0.405	0.226
CIO-M	0.684	0.669	0.130
CIO-L	0.716	0.686	0.107
SIO-H	0.574	0.496	0.212
SIO-M	0.457	0.419	0.259
SIO-L	0.490	0.366	0.179

Initially it was expected that capped nanoparticles would exhibit more defined and prominent influences on Sorbitol that would be easier to quantify in trends than for uncapped nanoparticles. Current data

collected, and shown for clarity in Table 4, reveals the uncapped nanoparticles displayed trends with respect to concentration. Higher concentrations led to lower melting temperatures and lower peak heat flows in the peak and secondary melt temperatures. The induced peak increased in heat flow as the concentration increased. The TX-100 capped particles did not display definitive trends in either of these metrics. These trends break down due to the medium concentration. It is currently unclear if this sample is an outlier, representing a nanocomposite lacking quality dispersion or if the TX-100 capping agent does not lead to clear trends in melting temperature or peak heat flow.

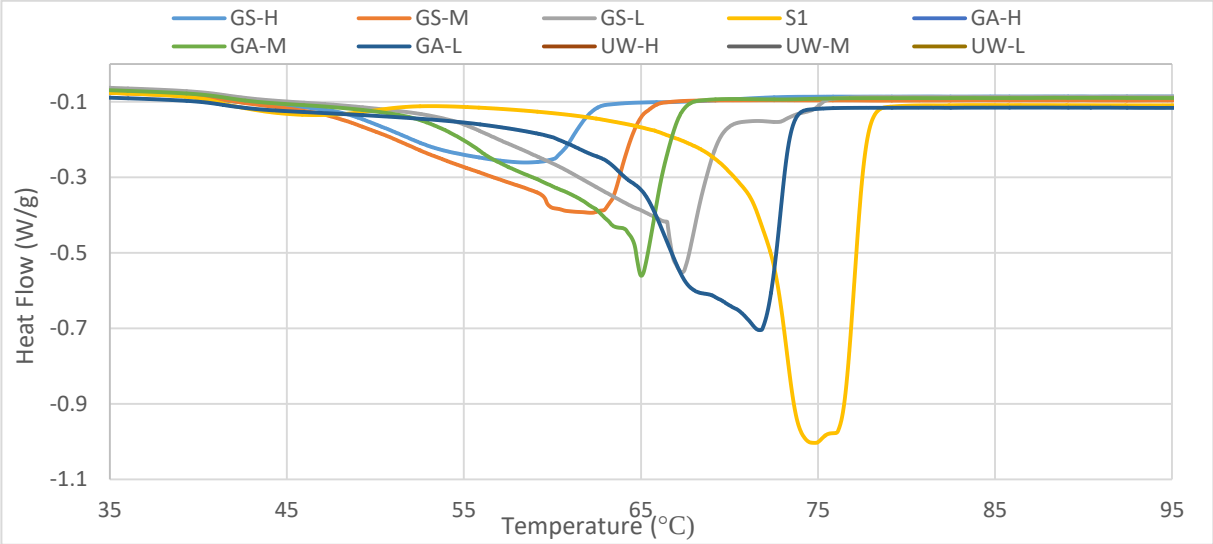

Figure 18. Heat flow vs temperature for graphene oxide nanocomposites.

Graphene oxide nanocomposites demonstrate drastic differences in melting temperature and heat flow when compared to the control sorbitol. Graphene oxide nanocomposites do not induce the third high temperature peak in the nanocomposite at a high rate. Even the samples that do show this peak do not exhibit the prominence seen in gold or iron oxide samples. This could be a result of the major difference in particle size/shape. The nanoparticle flakes are much larger than the spherical iron oxide or gold particles. This will change how the lattice structure is affected because the large flakes will disrupt a larger localized region, but there will also be larger distance between particle affected areas. The particles are altering the localized areas drastically which is likely causing the large change in melting temperature and significant reduction in heat flow.

Table 5. Peak Heat Flow and Melting Temperature values for graphene oxide nanocomposites.

Melting Temperatures (°C)

Sample	Peak Melt	Secondary Melt	Tertiary Melt	Total Melt Range
S1	74.77	76.06	NA	19.83
GS-H	58.41	53.02	67.28	33.29
GS-M	62.18	59.94	NA	25.37
GS-L	67.32	66.26	72.81	33.51
GA-H	59.57	NA	NA	27.7
GA-M	65.04	63.51	NA	27.39
GA-L	71.72	68.45	NA	32.68
UW-H	60.92	50.16	NA	31.21
UW-M	68.3	63.75	NA	29.65
UW-L	68.02	61.04	77.09	34.79

Peak Heat Flows (W/g)

Sample	Peak	Secondary	Tertiary
S1	0.959	0.975	NA
GS-H	0.293	0.22	0.1
GS-M	0.421	0.38	NA
GS-L	0.571	0.416	0.153
GA-H	0.312	NA	NA
GA-M	0.588	0.431	NA
GA-L	0.663	0.607	NA
UW-H	0.32	0.127	NA
UW-M	0.547	0.314	NA
UW-L	0.656	0.296	0.104

Graphene oxide samples were created to view the differences between concentration and nanoparticle size on key thermal properties. Table 5 shows the melting temperature and heat flow values for graphene oxide nanocomposites. Increased concentration generally leads to reduction in melting temperature. There is not a temperature change between UW-L and UW-M. This may result from less than ideal dispersion quality in UW-L or could be a result of variability in the particle size as the particles may be of any size less than 15 μm for this specific particle. The peak heat values across all particle sizes decrease as a result of increased particle concentration. Particle size does not appear to have an affect over the peak heat flow values. Particle size does appear to be a factor in the peak heat flow, but does have influence over melting temperatures. Smaller particle sizes tend to result in lower temperatures.

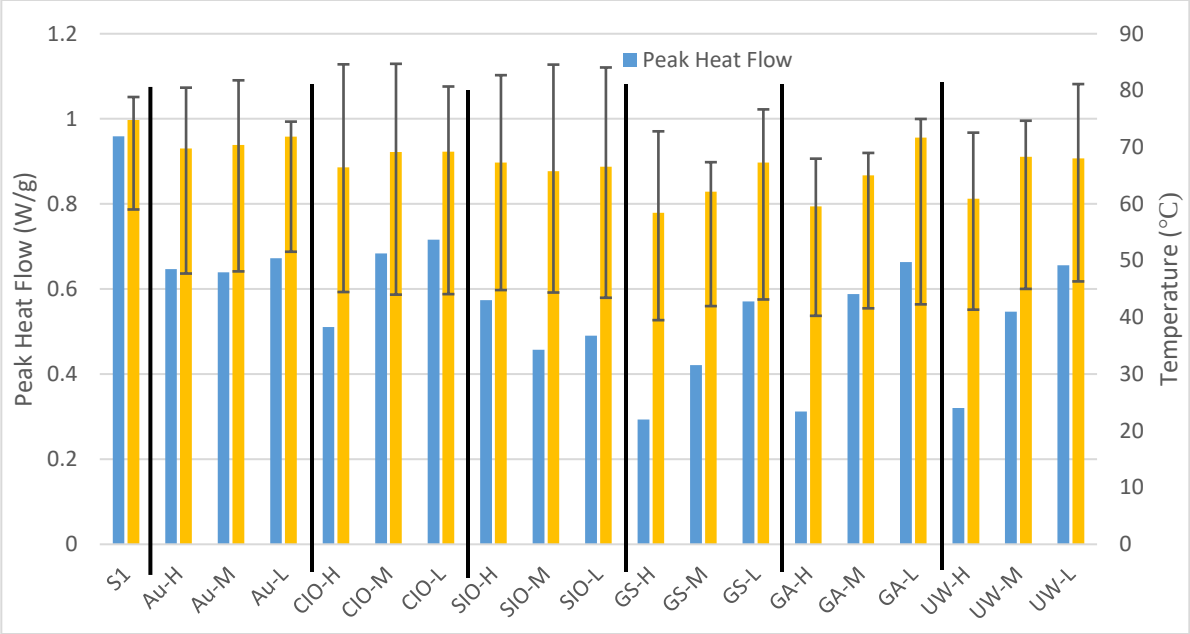

Figure 19. Visual comparison of peak heat flow and melting temperature for gold and iron oxide nanocomposites.

Gold and iron oxide nanocomposites are compared in Figure 19. The graph is divided into sections for each separate particle type. The gold samples experience less pronounced change in properties than the iron oxide samples. The peak heat flow in the gold samples does not change significantly with respect to concentration, but the uncapped iron oxide particles experience a large change in peak heat flow, increasing with lower concentrations. This change is even more drastic in the graphene oxide samples. All 3 graphene oxide particles sizes exhibit large changes in peak heat flow with respect to concentration. This can be related to the significant size difference of the graphene oxide flakes and the effect this has on the lattice structure. The changes influenced by the gold nanoparticles closely resemble those of the TX-100 capped nanoparticles. Though made with different capping agents, these particles resemble each other the most in structure and create similar augmentations as a result.

Latent Heat

Thermal energy storage in PCMs relies heavily on latent heat. The PCM's effectiveness depends heavily on the amount of energy it can absorb per unit mass. High latent heats allow for passive cooling to be effective at reduced spatial requirements. This metric must be balanced with thermal conductivity to create a PCM that can quickly absorb thermal energy and can store large quantities through the phase transition. The effect of nanoparticles on the latent heat is compared to the control material. The numerical values are displayed in ***Appendix B***, with corresponding nanoparticle characterizations for exact representation. The following graphs will interpret this data and connect the latent heat trends to the nanoparticle traits.

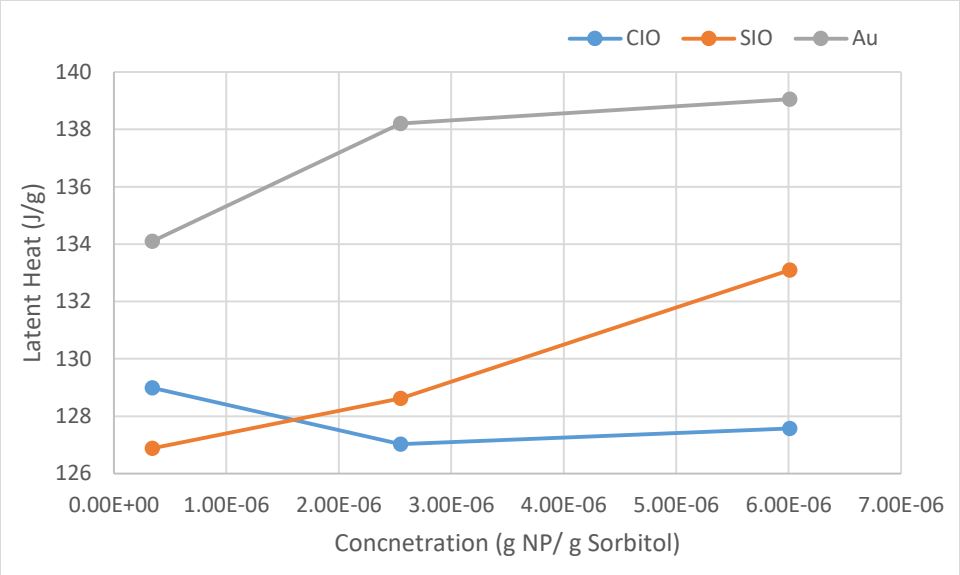

Figure 20. Latent heat comparison for iron oxide and gold nanocomposites.

Across all samples the latent heat value decreased by at least 45% as compared to the control Sorbitol sample. Plain Sorbitol has a measured latent heat value over 250 J/g. The closest nanocomposite latent heat value is seen in the highest gold concentration at 139 J/g. Gold nanocomposites show significantly higher latent heat values across all samples. Figure 20 shows the effect of nanoparticle concentration on the latent heat values for gold and both iron oxide nanocomposites. The nanocomposites with capping agents, gold and TX-100 capped iron oxide, displayed a similar trend in latent heat values increasing as a result of increasing nanoparticle concentration. Uncapped iron oxide nanocomposites lack a definitive latent heat trend with respect to particle concentration. The higher concentration uncapped nanocomposites have latent heats up to 5% less than the capped nanocomposite. The lack of trend and reduction in peak latent heat can be attributed to the capping chemistry not present. At lower concentrations of nanoparticles the uncapped samples have higher latent heat values. This could be a consequence of the composite not being affected by the extra mass of the capping agent. As the samples become more densely populated with nanoparticles, the lack of a capping agent allows the particles to begin agglomerating. This results in the higher concentration samples showing negative or undiscernible trends in latent heat values. Particle collection is negatively impacting the performance.

Graphene oxide nanocomposites are compared in Figure 21 to observe the effects of concentration and particle size on latent heat. These nanocomposites display strong correlation between nanoparticle concentration and latent heat. Higher nanoparticle concentrations lead to lower latent heat values, regardless of graphene oxide nanoparticle size. It is possible the size of the flakes relative to other nanoparticles in this study may lead to the decreasing trend. Each flake influences a region up to 3 orders of magnitude larger than either gold or iron oxide. Since these lattice disturbances are much larger, the latent heat likely would be preserved at concentrations that are not as disruptive to the structure on the macroscale. The influence of flake size is not as apparent as that of the concentration. The smallest particle size, 0.5 – 5 µm, consistently has the lowest latent heat, while the largest, less than 15 µm, and the medium, less than 10 µm, alternate which composite has the highest latent heat at each concentration. The small differences in these values suggests there may not be a reputable difference between these 3 nanoparticle sizes. It is possible this is a result of the particles being on the order of

microns rather than conventional nanoscale sized particles. At the micron size level the disturbance in the lattice structure might not be as susceptible to particle size variations.

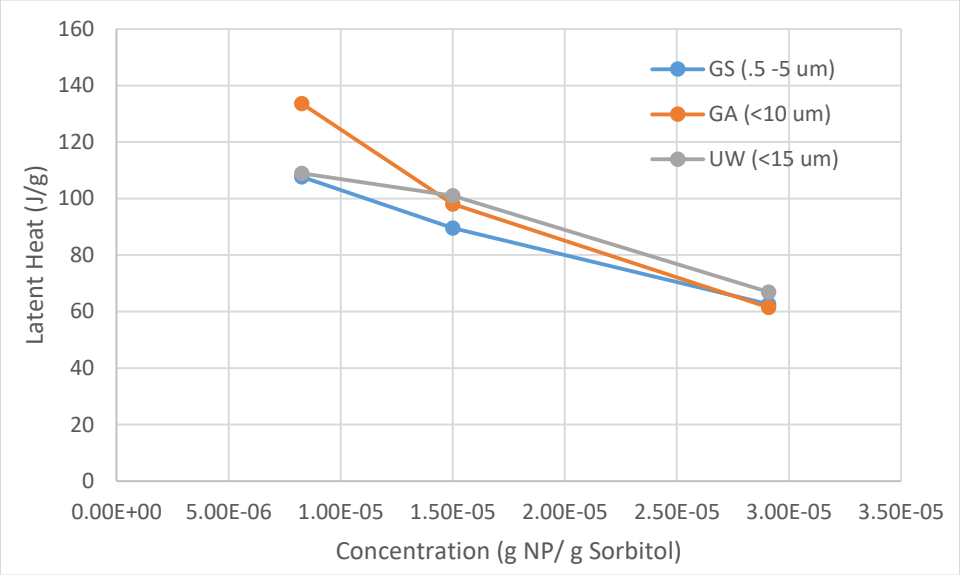

Figure 21. Latent heat comparison for particle size variation in graphene oxide nanocomposites.

When the latent heat values of these nanocomposites are compared together, the magnitude of changes arising from concentration difference is evident. Figure 22 displays the latent heat values and is grouped into specific particle type. The graphene oxide nanoparticles experience remarkably higher variability due to concentration. The influence of concentration plays a crucial role in the latent heat value for these nanocomposites. The other nanoparticle types do not experience the same magnitude of influence from their respected change in concentration. The latent heat results demonstrate the vast response differences Sorbitol can display depending on the characteristics of the included nanoparticle. Trends will lead to nanocomposite fine tuning of thermal properties through nanoparticle manipulation.

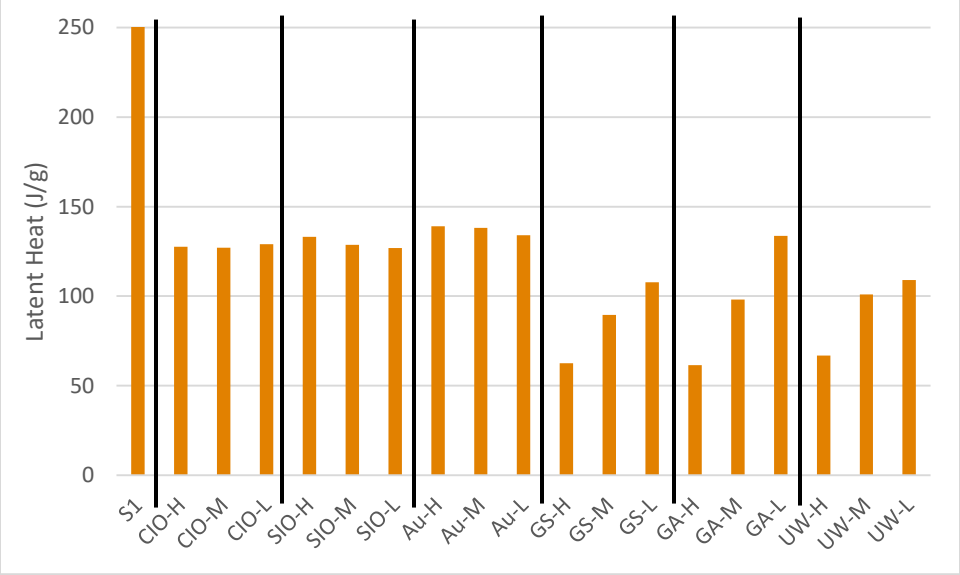

Figure 22. Latent heat comparison.

Specific Heat Capacity

It is important to understand how nanoparticle inclusion affects the specific heat capacity because this metric quantifies the amount of energy needed to increase the temperature of the material. This property can be used to determine the amount of energy needed to raise the temperature of the PCM high enough for a melt. Conductors have low specific heat values, needing small amounts of energy to increase in temperature. In a passive cooling system, materials with high specific heats will require larger time intervals to reach the phase transition, subsequently removing thermal energy from the system. The effect of nanoparticles on the specific heat is crucial to determining the energy input needed to raise the PCM to its melting temperature. Figure 23 shows a plot of the reversed normalized heat capacity as a function of temperature. The test provides the metric for solid and liquid state Sorbitol. During phase transitions, the system experiences an increase in the degrees of freedom resulting in large changes in the specific heat capacity. This study focuses on the influence of nanoparticles on the nanocomposite in both solid, tested at 35 °C, and liquid, tested at 100 °C, state without influence of the phase transition, but it will be important to understand how the width of the melting range affects the specific heat capacity for passive cooling design. ***Appendix E*** displays the graphs for all tested nanocomposites so the influence of the melt can be visually seen.

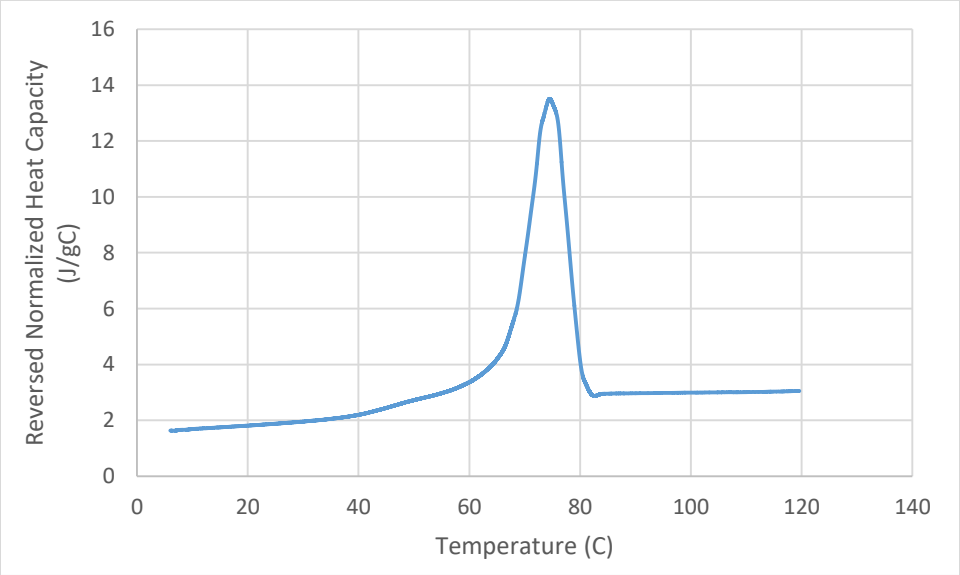

Figure 23. Specific Heat graph for control Sorbitol.

The specific heat capacity of Sorbitol in solid state is 2.05 (J/ g °C). The gold nanocomposites' specific heat value is at least 7% larger than that of Sorbitol. The uncapped iron oxide and TX-100 capped iron oxide nanoparticles' specific heat values are at least 29% and 37% larger than Sorbitol's respectively. Addition of nanoparticles substantially increases the energy needed to change the material's temperature by one degree. The iron oxide and gold nanocomposites show trends similar those seen in the latent heat measurements. This is expected as the thermal properties of the nanocomposite are closely related. Figure 24 shows the relationship between the nanoparticle concentration and the resulting specific heat capacity. The gold nanocomposites shows increases in the solid state specific heat resulting from higher concentrations. There is a 0.34 (J/ g °C) increase from the low to high gold concentrations. Gold nanocomposites also show an increase in the liquid state specific heat. This change is not as large, only change (0.08 J/ g °C). The gold composites experience the smallest change in specific

heat compared to Sorbitol's control measurement. The capped iron oxide particles also display increasing specific heat values in relation to increasing particle concentrations in solid state. The difference between high and low concentration specific heats is 0.26 (J/ g °C), less than that of gold. Unlike gold, the capped iron oxide nanocomposites see a more prominent change in specific heat in the liquid state, 0.27 (J/ g °C). This is interesting because the gold nanocomposites displayed a very small change, but the iron oxide, which have mimicked the thermal trends of gold, displayed almost identically the same increase in solid and liquid state. The uncapped iron oxide nanoparticles do not have a discernable connection between particle concentration and specific heat from the presented data. The specific heat values increase from the low to medium concentration, but then decrease when reaching the highest concentration. This may signify an improvement threshold for uncapped nanoparticles. A concentration between the medium and high presented here is likely the point at which nanoparticles become close enough in the sorbitol solution to begin the agglomeration process. This would lead to inconsistent results in influences on the nanocomposites characteristics. This would make sense given the uncapped nanocomposites resemble the capped iron oxide nanocomposites more closely at low concentrations before any potential trend breaks down at the higher concentration.

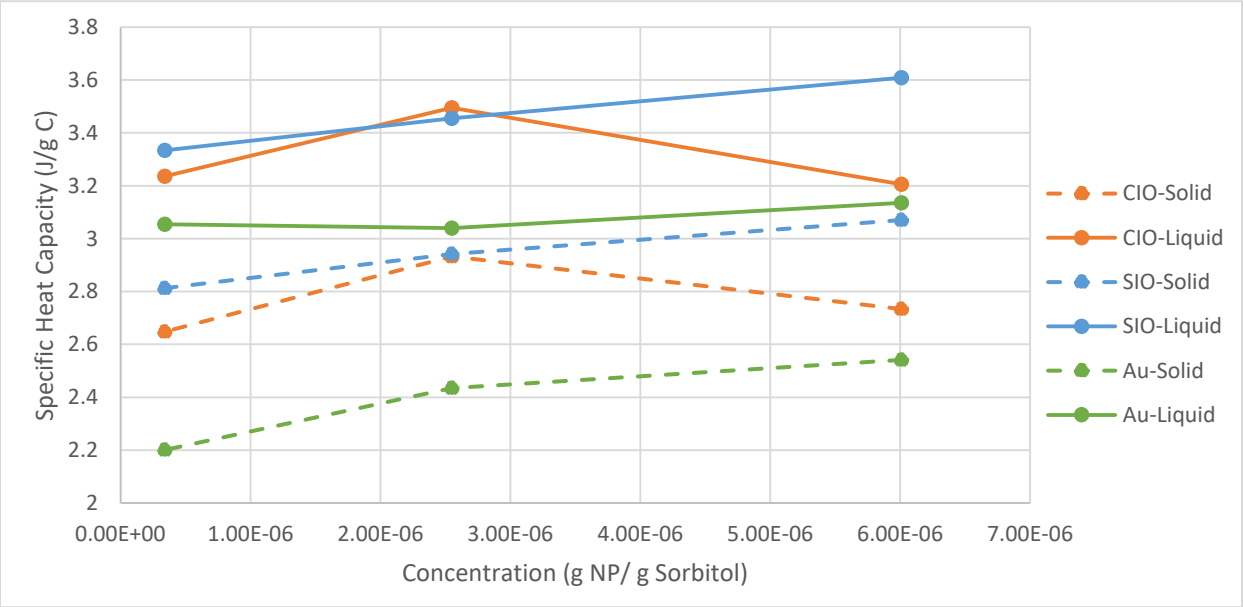

Figure 24. Specific heat capacity or gold and iron oxide nanocomposites with respect to particle concentration.

The differences between Sorbitol and the graphene oxide nanocomposites for specific heat values is comparable to that of the iron oxide nanocomposites. The graphene oxide samples specific heat capacity is shown in Figure 25. The graphene oxide particles experience at least a 37%, 28% increase, and 25% increase for the small, medium, and large nanoparticle sizes respectively as compared to Sorbitol. Graphene oxide nanocomposites appear to be affected by nanoparticle size rather than concentration. The small, 0.5 – 5 μm, and medium, less than 10 μm, show increasing specific heat when increasing from small to medium concentration, but show a leveling off or slight decrease in specific heat when going from the medium concentration to the large concentration. This may signify a limit was reached in-between the upper two concentrations leading to an excess of useful nanoparticles. Overall the change in specific heat from small to large concentration was the largest of any particle type for the medium particle size at 0.44 (J/ g °C). The change in the small particle size specific heat values was tied

with the gold samples for second highest at 0.34 (J/ g °C). Interestingly, the nanocomposite with the large particle size exhibited the opposite behavior as the other graphene oxide samples. At low concentration the sample had the highest specific heat of the graphene oxide samples. It then deceased in value from low to medium concentration. Like in the two smaller particle samples, the UW sample seems to have reached a barrier where the trend breaks down. From medium to high concentration, there was a notable increase of 0.27 (J/ g °C) in specific heat. From the thermal characterizations, it can be inferred the large particle sizes are not as effective at developing controllable trends. This is likely attributed to the difficulty in controlling the consistency of sizing in graphene oxide flakes. The nanoparticles are designed not to be larger than a certain size, but the creation process leaves a larger variation in size for samples with larger particle sizes.

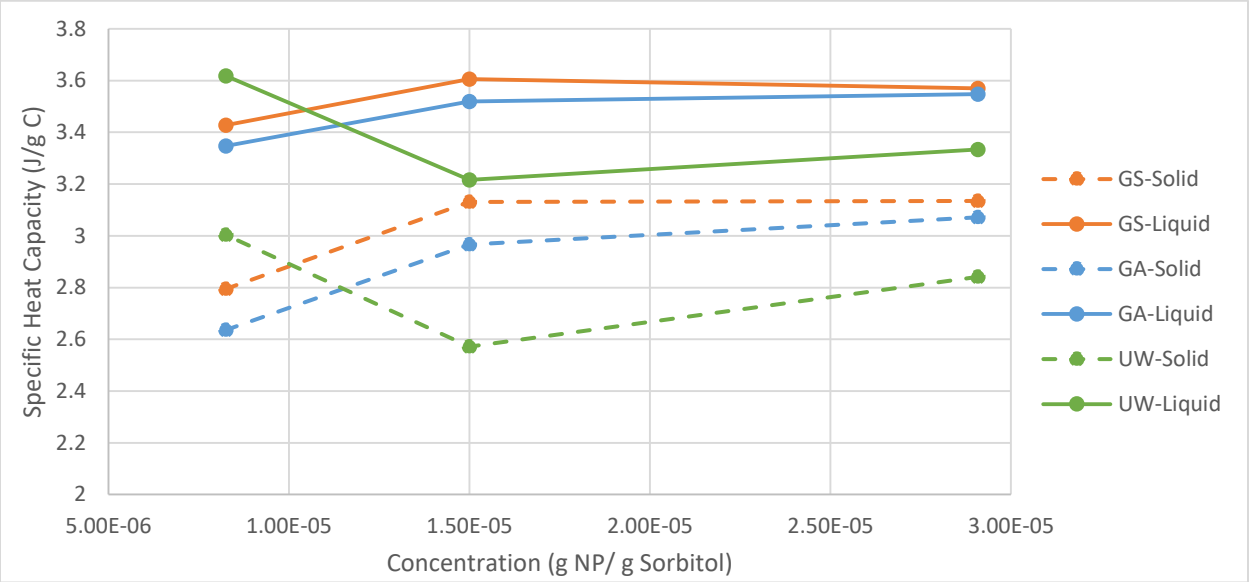

Figure 25. Specific heat capacity for graphene oxide nanocomposites with respect to particle concentration.

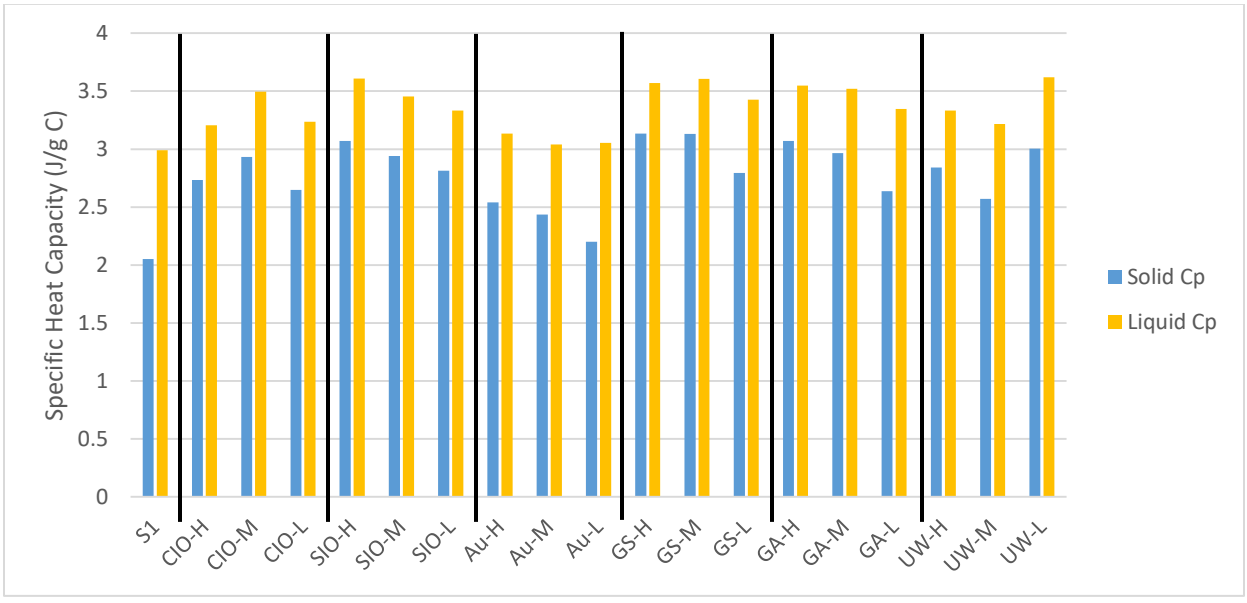

Figure 26. Specific heat comparison for all nanocomposites, solid and liquid state.

For specific heat capacity, the most well defined trends appeared in the TX-100 capped and medium sized graphene oxide nanocomposites. Figure 26 shows a comparison across all samples. This graphic shows how the nanoparticles have greatly increased the specific heat of the composites. This metric does not contain well defined trends as seen in the latent heat measurements. It is not clear why specific heat did not change in similar trends as the latent heat. The uncapped nanoparticles displayed similar lack of trends, but the graphene oxide samples did not all react to nanoparticle inclusion the same. This is interesting because the graphene oxide nanocomposites showed similar trends in latent heat regardless of particle size. Overall, the specific heat measurements showed promising trends for determining the effect of nanoparticle concentration and type. More work needs to be done on how size affects this property to confirm the results shown here. The reversed normalized heat graphs will prove useful for an in-depth study of the change in specific heat with respect to temperature for passive cooling system considerations.

Conclusions

Phase change materials offer a promising option for temperature spike alleviation in passive cooling systems. Ideal candidates for energy absorption through phase transitions must have high latent heats and thermal conductivities to quickly remove large amounts of heat from the material. Organic PCMs, such as Sorbitol, have large latent heats and melting temperatures in the ideal range for cooling systems in electronics, but do not have ideal thermal conductivity. Nanoparticles have been shown to increase the thermal conductivity in Sorbitol and offer the opportunity to enhance this PCM. This study examined how nanoparticle type, capping chemistry, size, and concentration augment key thermal and crystalline characteristics of the resulting nanocomposites. The results showed the importance of these nanoparticle characteristics on altering the various properties and outlined some trends that were seen.

Introduction of nanoparticles alters the lattice spacing of the composite, leading to shifts in Sorbitol's phases. In some instances, new phases were introduced. Changes in lattice spacing were affected by nanoparticle type. Graphene oxide was the only nanoparticle to cause the lattice spacing to increase. Gold and iron oxide nanoparticles all led to compression of the lattice spacing. In the iron oxide comparison, the TX-100 capping agent played a significant role in the magnitude of the decrease in lattice spacing, 3 times less impactful than uncapped nanoparticles. Trends in thermal properties were defined as a result of nanoparticle properties. The importance of an effective capping agent was shown in this study. Controllable trends were seen in the iron oxide and gold particles with capping agents. These samples had strong correlation between concentration and the change in each thermal property. Trends were not as clear for the uncapped iron oxide samples. It is important to note the variability in property trends the uncapped iron oxide sample displayed. The lack of a capping agent significantly affected the particle to Sorbitol interactions and resulted in trends that were not consistent across all characterization methods. This can be attributed to agglomeration occurring at higher concentrations, sample that did not align with any trend most often. Particle size played an important role in the graphene oxide samples. The larger particles created less clear trends in the thermal properties. This is likely because larger particles disrupted a larger region of the lattice structure. Too much disruption can leave a negative impact creating large regions that do not possess the strong thermal properties such as latent heat of the host material. As a whole the graphene oxide nanoparticles performed less ideally than the capped iron oxide or gold samples. It is possible better results would be recorded from graphene oxide samples with significantly smaller flake sizes as the lattice structure would be affected in the same way. This would create more nanoparticles with less spacing between, where each particle

affects a smaller region. The gold samples seem to be most favorable for controlling the thermal properties. They are well dispersed because of their trisodium citrate capping agent and are smaller sized particles, which appears to be beneficial.

Though these efforts show promise for developing a Sorbitol based PCM cooling system, there are many facets left to explore in this area. The next step in fully understanding the nanoparticle effects on these samples is to characterize the impact on their thermal conductivity directly. This will help determine the balancing effect between latent heat and conduction necessary for picking an ideal system. The work could also be further expanded by including different types of carbon based nanoparticles to compare the differences these different shapes and forms create. Combining sugar alcohols can drastically change the melting temperature of the final composite. How nanoparticles interact in a composite with multiple base PCMs will be important to increasing the range of operation for these composites. Electronic systems are highly diverse and require adaptable systems to successfully cool at different temperatures and energy rates. Improving the ability to vary the properties of a PCM will lead to the diversity needed to implement a PCM based cooling system effectively in the electronics industry.

Acknowledgements

The author would like to thank the University of Arkansas for providing the facilities and opportunities to pursue this subject. The University was instrumental in providing testing facilities and access to review content. The Honors College receives special recognition for awarded grant funding that was integral supply the necessary resources to create these samples. The University of Arkansas faculty was crucial in adding with all aspects of this study. Hayden Carlton is acknowledged for his contributions through many forms. Hayden provided iron oxide nanoparticles for nanoparticle inclusion, as well as assisted in many data collection endeavors. Hayden is also responsible for all training that was needed to collect this data. Fernando Ibanez is recognized for contributing gold nanocomposites that were tested in this study. The entirety of the EMPIRE research group led by Dr. Huitink was instrumental in providing insights and support throughout this project. Dr. Huitink is recognized as the key mentor and was important in providing guidance throughout the project. Without his support and vision, this study would not have obtained the results necessary to understand the topic in question.

Appendixes

Appendix A

Gold Nanoparticle Calculation Matrix

Inputs

Desired NP size	14	nm
Concentration ratio	0.197835	
Expected Absorption Wavelength	522	

Curve fit for Turkevich Method

y = 9.9514 * exp(1.7254 * x)
x = concentration ratio
y = nanoparticle size (nm)

1st Solution

Concentration HAuCl4	0.01	M
Volume HAuCl4	50	ml
HAuCl4 mass	0.196915	g

HAuCl4 Molar Mass	393.83	g
Tri-Sodium Citrate Molar Mass	258.07	g

Material Constants
Initial Conditions
Inputs
Outputs

2nd Solution

Volume Tri Sodium Cit Sol	50	ml
Concentration Tri -Sodium Citrate	0.050547	M
Tri-Sodium Citrate mass	0.652236	g

Heated Solution

Volume HAuCl4 Added to Heat	1.3	ml
Volume Deionized Water Added to Heat	48.7	ml
Concentration HAuCL4 Heated Sol	0.000260	M

Final Solution

Volume Final Solution	60	ml
Volume Tri Sodium Cit Sol Added to Final Sol	10	ml
Volume Heated Solution	50	ml
Final HauCl4 Concentration	0.000217	M
Final Tri-Sodium-Citrate Concentration	0.008425	M

Figure 27. Calculations for gold nanoparticle sizing.

Appendix B

Table showing the change in lattice structure calculated using Bragg's Law.

Table 6. Calculations for lattice spacing (d) of graphene oxide nanocomposite.

		Sorbitol			GA-L Nanocomposite				
λ	n	2θ	d	Peak Intensity rank	2θ	d	Peak Intensity rank	Shift in d	Units
1.51E-10	1	8	1.07908E-09	18					Å
1.51E-10	1	9.36	9.22569E-10	17	9.7	8.90305E-10	10	-0.32264	Å
1.51E-10	1	12.44	6.94744E-10	3	12.35	6.99787E-10	5	0.05043	Å
1.51E-10	1	14.1	6.13295E-10	4	14.05	6.15466E-10	8	0.02172	Å
1.51E-10	1	17.12	5.05714E-10	5	16.95	5.10748E-10	12	0.05034	Å
1.51E-10	1	19.54	4.43582E-10	2	19.15	4.52529E-10	1	0.08947	Å
1.51E-10	1	20.64	4.20178E-10	8	20.65	4.19976E-10	4	-0.00201	Å
1.51E-10	1	21.84	3.97349E-10	1	21.75	3.98973E-10	2	0.01624	Å
1.51E-10	1	23.86	3.64136E-10	6	23.8	3.65041E-10	3	0.00905	Å
1.51E-10	1	25.08	3.46687E-10	7					Å
1.51E-10	1	26.94	3.23149E-10	11	26.65	3.26600E-10	13	0.03452	Å
1.51E-10	1	29.9	2.91783E-10	12	29.7	2.93703E-10	14	0.01920	Å
1.51E-10	1	32.18	2.71600E-10	10	32.2	2.71435E-10	11	-0.00164	Å
1.51E-10	1	33.5	2.61187E-10	14	33.55	2.60808E-10	7	-0.00378	Å
1.51E-10	1	34.76	2.51996E-10	13	35.45	2.47244E-10	15	-0.04752	Å
1.51E-10	1	36.48	2.40490E-10	16	36.45	2.40682E-10	16	0.00191	Å
1.51E-10	1	37.68	2.33096E-10	15	38.45	2.28600E-10	9	-0.04497	Å
1.51E-10	1	42.88	2.05930E-10	9	42.3	2.08622E-10	6	0.02692	Å
							Average shift =	-0.00685	Å

Table 7. Calculations for lattice spacing (d) of gold nanocomposite.

		Sorbitol			Au-7 Nanocomposite				
λ	n	2θ	d	Peak Intensity rank	2θ	d	Peak Intensity rank	Shift in d	Units
1.51E-10	1	8.00	1.07908E-09	18					Å
1.51E-10	1	9.36	9.22569E-10	17					Å
1.51E-10	1	12.44	6.94744E-10	3	12.68	6.81647E-10	3	-0.13098	Å
1.51E-10	1	14.10	6.13295E-10	4	14.40	6.00583E-10	4	-0.12712	Å
1.51E-10	1	17.12	5.05714E-10	5	17.38	4.98205E-10	11	-0.07509	Å
1.51E-10	1	19.54	4.43582E-10	2	19.70	4.40014E-10	1	-0.03568	Å
1.51E-10	1	20.64	4.20178E-10	8	21.00	4.13053E-10	13	-0.07124	Å
1.51E-10	1	21.84	3.97349E-10	1	22.16	3.91681E-10	2	-0.05668	Å
1.51E-10	1	23.86	3.64136E-10	6	24.16	3.59681E-10	6	-0.04456	Å
1.51E-10	1	25.08	3.46687E-10	7	25.30	3.43720E-10	7	-0.02966	Å
1.51E-10	1	26.94	3.23149E-10	11	27.22	3.19886E-10	9	-0.03262	Å
1.51E-10	1	29.90	2.91783E-10	12	30.20	2.88951E-10	12	-0.02832	Å
1.51E-10	1	32.18	2.71600E-10	10	32.50	2.68996E-10	5	-0.02603	Å
1.51E-10	1	33.50	2.61187E-10	14	33.88	2.58342E-10	7	-0.02845	Å
1.51E-10	1	34.76	2.51996E-10	13	35.18	2.49080E-10	15	-0.02915	Å
1.51E-10	1	36.48	2.40490E-10	16					Å
1.51E-10	1	37.68	2.33096E-10	15	38.26	2.29692E-10	14	-0.03404	Å
1.51E-10	1	42.88	2.05930E-10	9	42.84	2.06113E-10	9	0.00183	Å
							Average shift =	-0.04985	Å

Table 8. Calculations for lattice spacing (d) in uncapped iron oxide nanocomposite.

		Sorbitol			CIO Nanocomposite				
λ	n	2θ	d	Peak Intensity rank	2θ	d	Peak Intensity rank	Shift in d	Units
1.51E-10	1	8	1.07908E-09	18					Å
1.51E-10	1	9.36	9.22569E-10	17					Å
1.51E-10	1	12.44	6.94744E-10	3	12.92	6.69037E-10	4	-0.25707	Å
1.51E-10	1	14.1	6.13295E-10	4	14.64	5.90790E-10	5	-0.22505	Å
1.51E-10	1	17.12	5.05714E-10	5	17.68	4.89817E-10	11	-0.15897	Å
1.51E-10	1	19.54	4.43582E-10	2	20.04	4.32624E-10	1	-0.10959	Å
1.51E-10	1	20.64	4.20178E-10	8	21.08	4.11503E-10	9	-0.08674	Å
1.51E-10	1	21.84	3.97349E-10	1	22.36	3.88221E-10	2	-0.09127	Å
1.51E-10	1	23.86	3.64136E-10	6	24.4	3.56196E-10	3	-0.07941	Å
1.51E-10	1	25.08	3.46687E-10	7	25.78	3.37426E-10	8	-0.09261	Å
1.51E-10	1	26.94	3.23149E-10	11	27.78	3.13561E-10	7	-0.09588	Å
1.51E-10	1	29.9	2.91783E-10	12	30.46	2.86542E-10	13	-0.05241	Å
1.51E-10	1	32.18	2.71600E-10	10	32.9	2.65815E-10	6	-0.05785	Å
1.51E-10	1	33.5	2.61187E-10	14	33.7	2.59681E-10	15	-0.01506	Å
1.51E-10	1	34.76	2.51996E-10	13	35.52	2.46772E-10	14	-0.05223	Å
1.51E-10	1	36.48	2.40490E-10	16	36.84	2.38221E-10	12	-0.02270	Å
1.51E-10	1	37.68	2.33096E-10	15	38.22	2.29923E-10	16	-0.03173	Å
1.51E-10	1	42.88	2.05930E-10	9	43.4	2.03580E-10	10	-0.02350	Å
							Average shift =	-0.09075	Å

Table 9. Calculations for lattice spacing (d) in TX-100 capped iron oxide nanocomposite.

		Sorbitol			SIO Nanocomposite				
λ	n	2θ	d	Peak Intensity rank	2θ	d	Peak Intensity rank	Shift in d	Units
1.51E-10	1	8	1.07908E-09						Å
1.51E-10	1	9.36	9.22569E-10						Å
1.51E-10	1	12.44	6.94744E-10		12.6	6.85957E-10		-0.08787	Å
1.51E-10	1	14.1	6.13295E-10		14.22	6.08145E-10		-0.05149	Å
1.51E-10	1	17.12	5.05714E-10		17.16	5.04544E-10		-0.01170	Å
1.51E-10	1	19.54	4.43582E-10		19.7	4.40014E-10		-0.03568	Å
1.51E-10	1	20.64	4.20178E-10		20.74	4.18174E-10		-0.02004	Å
1.51E-10	1	21.84	3.97349E-10		21.94	3.95560E-10		-0.01789	Å
1.51E-10	1	23.86	3.64136E-10		24.02	3.61746E-10		-0.02390	Å
1.51E-10	1	25.08	3.46687E-10		25.4	3.42389E-10		-0.04297	Å
1.51E-10	1	26.94	3.23149E-10		27.16	3.20580E-10		-0.02569	Å
1.51E-10	1	29.9	2.91783E-10		29.98	2.91022E-10		-0.00761	Å
1.51E-10	1	32.18	2.71600E-10		32.5	2.68996E-10		-0.02603	Å
1.51E-10	1	33.5	2.61187E-10		33.92	2.58046E-10		-0.03141	Å
1.51E-10	1	34.76	2.51996E-10		35	2.50321E-10		-0.01674	Å
1.51E-10	1	36.48	2.40490E-10		36.6	2.39729E-10		-0.00762	Å
1.51E-10	1	37.68	2.33096E-10		39.64	2.22001E-10		-0.11096	Å
1.51E-10	1	42.88	2.05930E-10		43.02	2.05292E-10		-0.00639	Å
							Average shift =	-0.03275	Å

Appendix C

XRD Plots

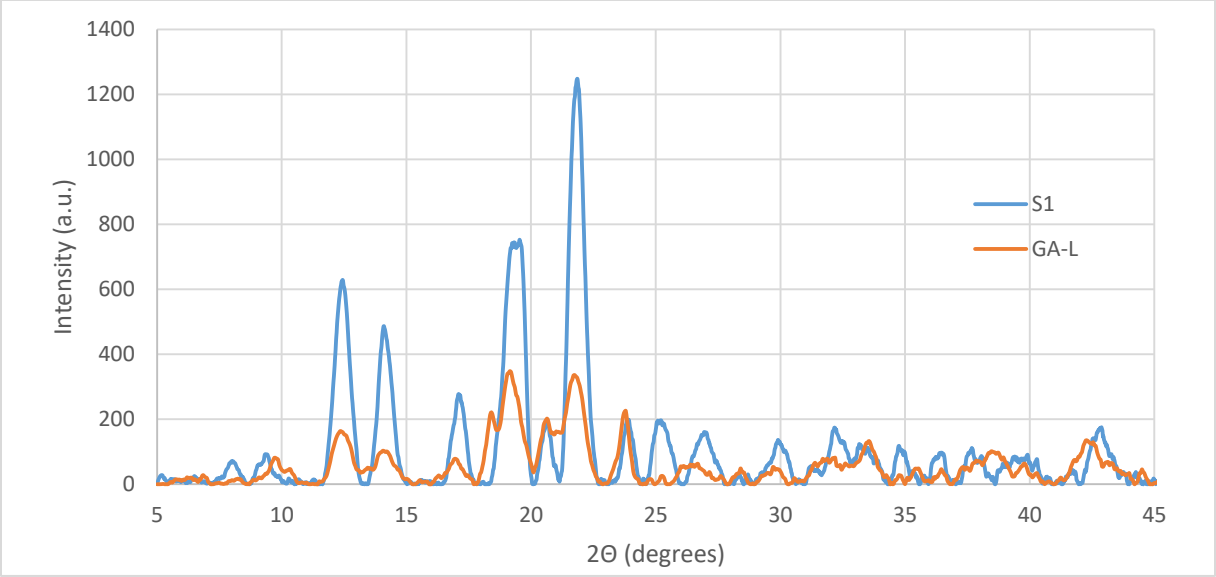

Figure 28. XRD plot for Sorbitol and graphene oxide nanocomposite comparison.

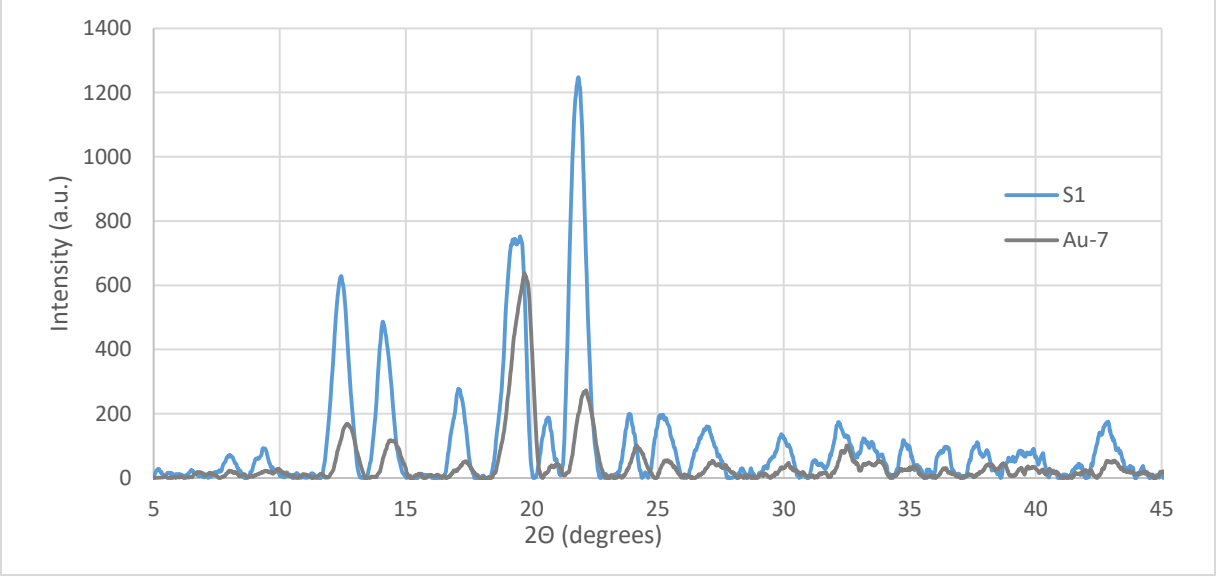

Figure 29. XRD plot for Sorbitol and gold nanocomposite comparison.

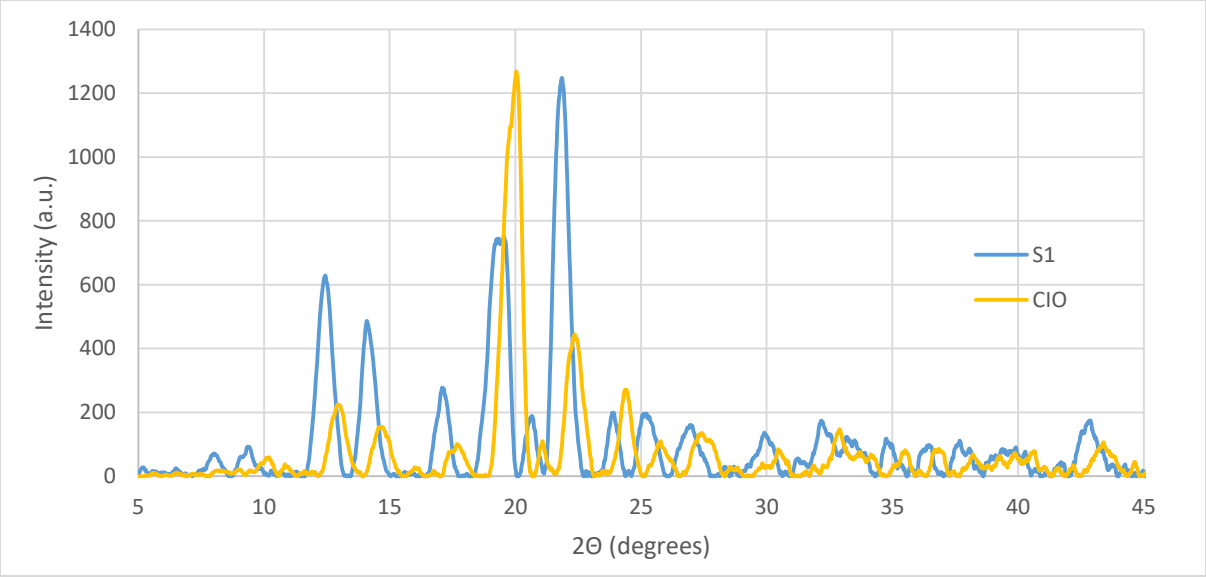

Figure 30. XRD plot for Sorbitol and uncapped iron oxide nanocomposite comparison.

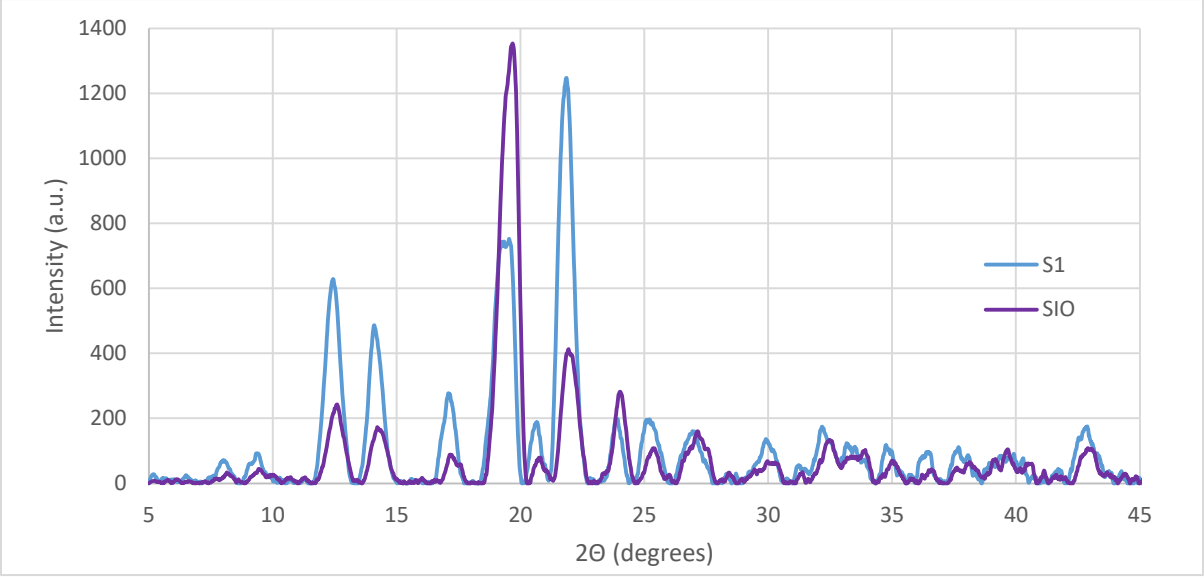

Figure 31. XRD plot for Sorbitol and TX-100 capped iron oxide nanocomposite comparison.

Appendix D

Table for Latent heat values with respect to nanoparticle characterizations.

Table 10. Latent heat values for all nanocomposites.

Sample	Nanoparticle Size	Capping Agent	Conc. NP g/ Sorbitol g	Latent Heat (J/g)
S1	NA	NA	0	250.42
CIO-H	~15 nm	Uncapped	6.01E-06	127.57
CIO-M	~15 nm	Uncapped	2.55E-06	127.03
CIO-L	~15 nm	Uncapped	3.40E-07	128.99
SIO-H	~15 nm	TX-100	6.01E-06	133.1
SIO-M	~15 nm	TX-100	2.55E-06	128.62
SIO-L	~15 nm	TX-100	3.40E-07	126.88
Au-H	14 nm	Trisodium Citrate	6.01E-06	139.05
Au-M	14 nm	Trisodium Citrate	2.55E-06	138.2
Au-L	14 nm	Trisodium Citrate	3.40E-07	134.1
GS-H	.5 - 5 µm	Trisodium Citrate	2.91E-05	62.631
GS-M	.5 - 5 µm	Trisodium Citrate	1.50E-05	89.539
GS-L	.5 - 5 µm	Trisodium Citrate	8.26E-06	107.68
GA-H	< 10 µm	Trisodium Citrate	2.91E-05	61.544
GA-M	< 10 µm	Trisodium Citrate	1.50E-05	98.063
GA-L	< 10 µm	Trisodium Citrate	8.26E-06	133.59
UW-H	< 15 µm	Trisodium Citrate	2.91E-05	66.886
UW-M	< 15 µm	Trisodium Citrate	1.50E-05	100.97
UW-L	< 15 µm	Trisodium Citrate	8.26E-06	108.92

Appendix E

Table for specific heat values in solid and liquid state. Table also contains the average rate of change for the specific heat values as a function of temperature.

Table 11. Specific heat values for all nanocomposites.

Sample	Conc. NP g/ Sorbitol g	Cp (J/g°C) @ 35 °C	Cp (J/g°C) @ 100 °C	dCp/dT Solid (J/g°C)	dCp/dT Liquid (J/g°C)
S1	0	2.05228	2.99062	0.0135629	0.0024437
CIO-H	6.01E-06	2.73415	3.2054	0.0177172	0.00252954
CIO-M	2.55E-06	2.93261	3.49471	0.0157387	0.00145247
CIO-L	3.40E-07	2.64802	3.23611	0.0162261	0.00226321
SIO-H	6.01E-06	3.07022	3.60894	0.0177771	0.00218905
SIO-M	2.55E-06	2.94123	3.45447	0.0156206	0.000762544
SIO-L	3.40E-07	2.81272	3.33337	0.0168603	0.00217334
Au-H	6.01E-06	2.54148	3.13531	0.0173092	0.00130226
Au-M	2.55E-06	2.43523	3.03996	0.0155854	0.00135986
Au-L	3.40E-07	2.20096	3.05388	0.0139542	0.0015437
GS-H	2.91E-05	3.13489	3.57	0.00689961	0.00252816
GS-M	1.50E-05	3.13118	3.60551	0.0103188	0.00228845
GS-L	8.26E-06	2.79502	3.42764	0.0108341	0.00244701
GA-H	2.91E-05	3.07155	3.54779	0.00671016	0.00225903
GA-M	1.50E-05	2.96627	3.51956	0.00953042	0.0023956
GA-L	8.26E-06	2.63624	3.34719	0.00671016	0.00210012
UW-H	2.91E-05	2.84127	3.33325	0.00747681	0.00201693
UW-M	1.50E-05	2.57167	3.21657	0.00848414	0.00237219
UW-L	8.26E-06	3.00319	3.61878	0.0115874	0.001957

Appendix F

Reversing normalized heat flow plots for specific heat calculations

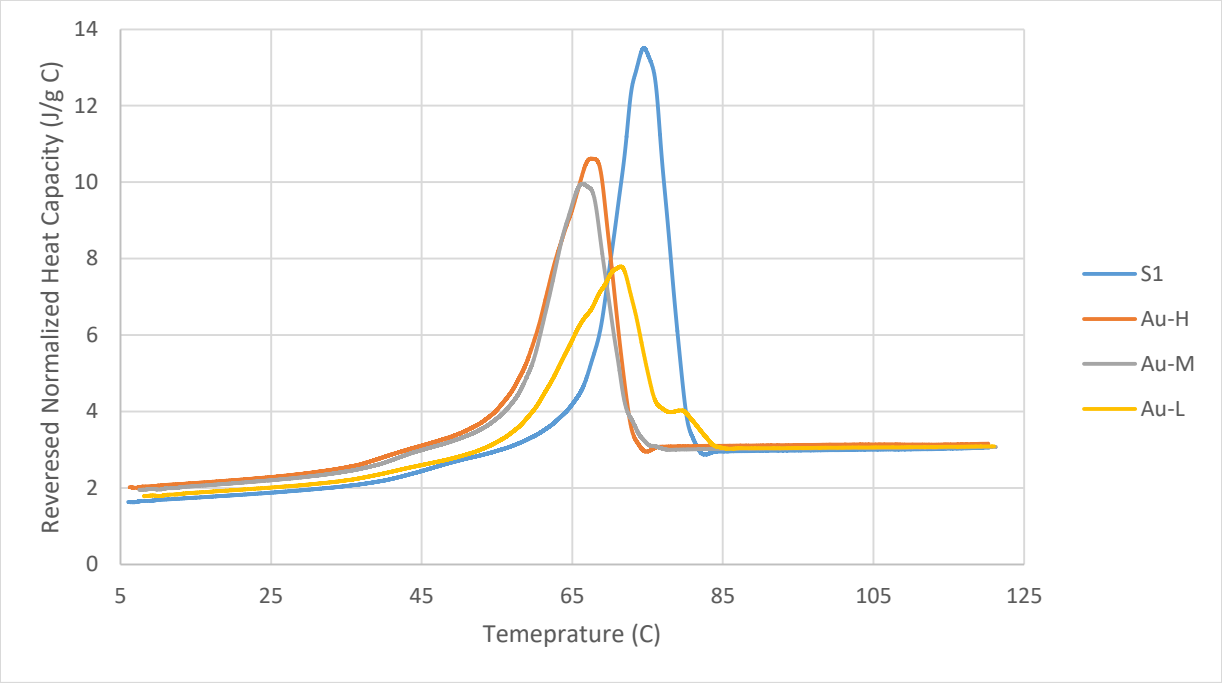

Figure 32. Specific heat capacity curve for gold nanocomposites.

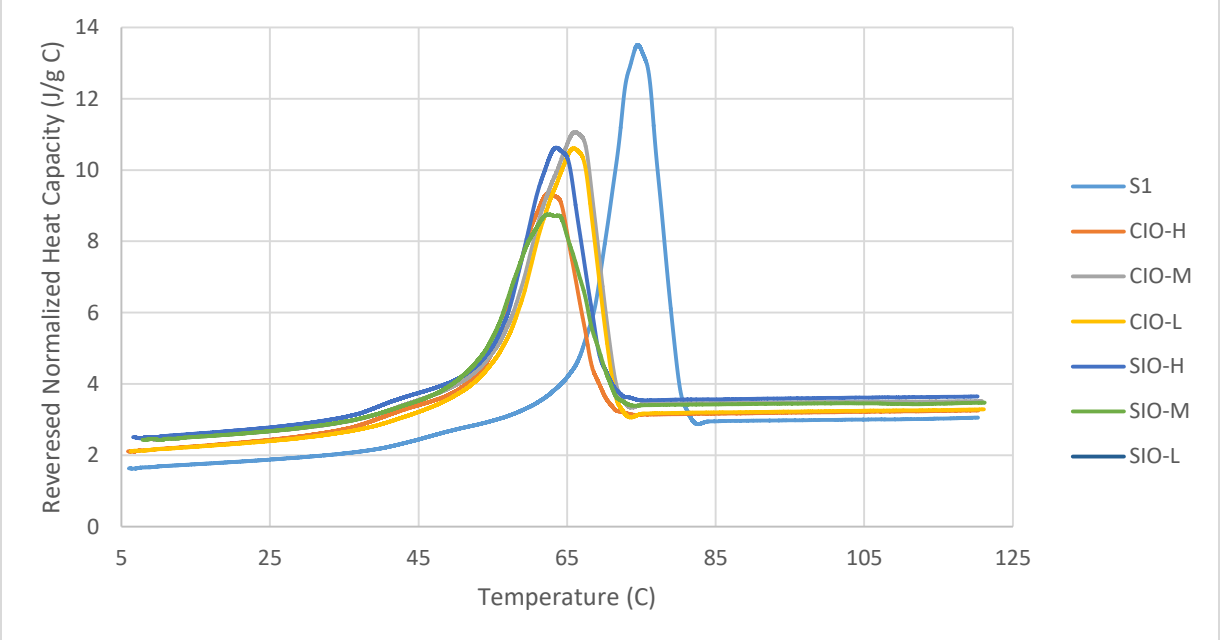

Figure 33. Specific heat capacity curves for iron oxide nanocomposites.

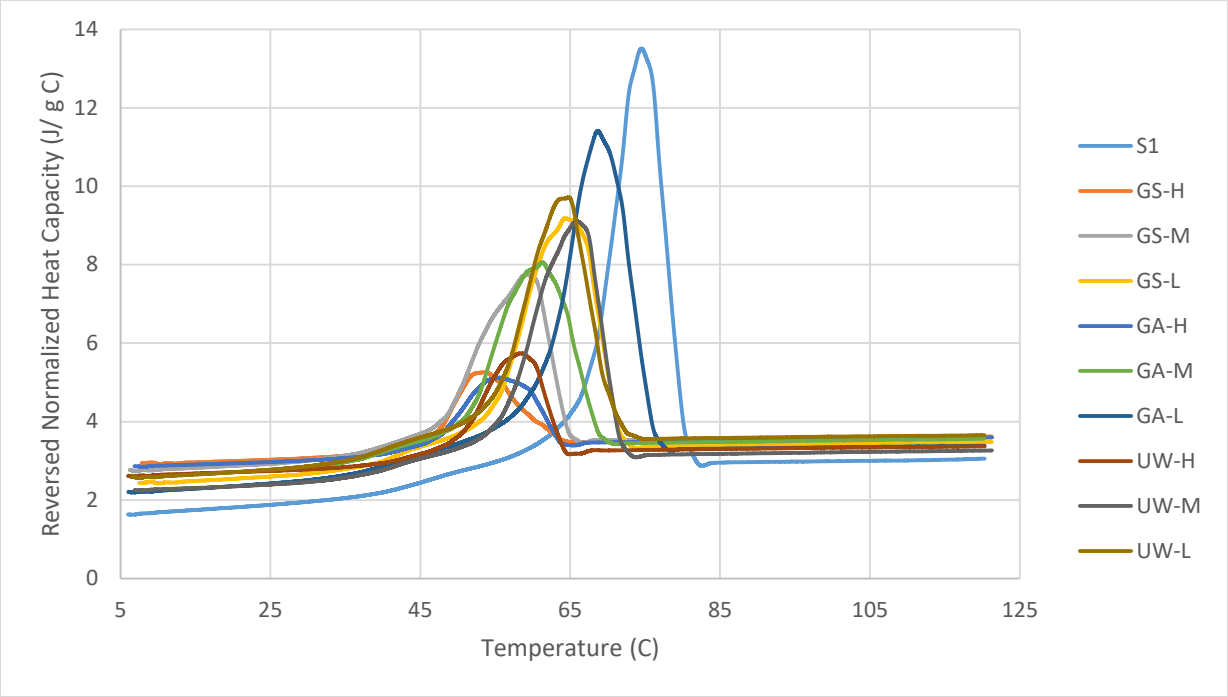

Figure 34. Specific heat capacity curves for graphene oxide nanocomposites.

References

[1] X. Liu, C. Marbut, D. Huitink, G. Feng, and A. S. Fleischer, “Influence of crystalline polymorphism on the phase change properties of sorbitol-Au nanocomposites,” Mater. Today Energy, vol. 12, pp. 379–388, 2019.

[2] N. Şahan, M. Fois, and H. Paksoy, “Improving thermal conductivity phase change materials—A study of paraffin nanomagnetite composites,” *Sol. Energy Mater. Sol. Cells*, vol. 137, pp. 61–67, 2015.

[3] N. Sahan and H. O. Paksoy, “Thermal enhancement of paraffin as a phase change material with nanomagnetite,” *Sol. Energy Mater. Sol. Cells*, vol. 126, pp. 56–61, 2014.

[4] R. K. Sharma, P. Ganesan, V. V Tyagi, H. S. C. Metselaar, and S. C. Sandaran, “Thermal properties and heat storage analysis of palmitic acid-TiO2 composite as nano-enhanced organic phase change material (NEOPCM),” *Appl. Therm. Eng.*, vol. 99, pp. 1254–1262, 2016.

[5] K. Kant, A. Shukla, and A. Sharma, “Advancement in phase change materials for thermal energy storage applications,” Sol. Energy Mater. Sol. Cells, vol. 172, pp. 82–92, 2017.

[6] Plamitic Acid

[7] T.-P. Teng, C.-M. Cheng, and C.-P. Cheng, “Performance assessment of heat storage by phase change materials containing MWCNTs and graphite,” Appl. Therm. Eng., vol. 50, no. 1, pp. 637–644, 2013.

[8] A. Karaipekli, A. Biçer, A. Sarı, and V. V. Tyagi, “Thermal characteristics of expanded perlite/paraffin composite phase change material with enhanced thermal conductivity using carbon nanotubes,” Energy Convers. Manag., vol. 134, pp. 373–381, 2017.

[9] R. J. Warzoha and A. S. Fleischer, “Improved heat recovery from paraffin-based phase change materials due to the presence of percolating graphene networks,” Int. J. Heat Mass Transf., vol. 79, pp. 314–323, 2014.

[10] M. Mehrali, S. T. Latibari, M. Mehrali, H. S. C. Metselaar, and M. Silakhori, “Shape-stabilized phase change materials with high thermal conductivity based on paraffin/graphene oxide composite,” Energy Convers. Manag., vol. 67, pp. 275–282, 2013.

[11] J. F. Li, W. Lu, Y. B. Zeng, and Z. P. Luo, “Simultaneous enhancement of latent heat and thermal conductivity of docosane-based phase change material in the presence of spongy graphene,” Sol. Energy Mater. Sol. Cells, vol. 128, pp. 48–51, 2014.

[12] S. Yu, S.-G. Jeong, O. Chung, and S. Kim, “Bio-based PCM/carbon nanomaterials composites with enhanced thermal conductivity,” Sol. Energy Mater. Sol. Cells, vol. 120, pp. 549–554, 2014.

[13] Turkevich, J., P. Cooper Stevenson, and J. Hillier, *A Study of the Nucleation and Growth Processes in the Synthesis of Colloidal Gold.* Vol. 11. 1951. 55-75.

[14] P. L. Hariani, M. Faizal, D. Setiabudidaya, *International Journal of Environmental Science and Development* **2013**, 4, 336.

[15] M. Mandal, S. Kundu, S. K. Ghosh, S. Panigrahi, T. K. Sau, S. M. Yusuf, T. Pal, *Journal of Colloid and Interface Science* **2005**, 286, 187.